

Born-Infeld AdS Black Holes Surrounded by Perfect Fluid Dark Matter

Behzad Eslam Panah ^{*}

*Department of Theoretical Physics, Faculty of Basic Sciences,
University of Mazandaran, P. O. Box 47416-95447, Babolsar, Iran*

Bilel Hamil [†]

*Laboratoire de Physique Mathématique et Physique Subatomique, LPMPS,
Faculté des Sciences Exactes, Université Constantine 1, Constantine, Algeria*

Manuel E. Rodrigues [‡]

*Faculdade de Física, Programa de Pós-Graduação em Física,
Universidade Federal do Pará, 66075-110, Belém, Pará, Brazil and
Faculdade de Ciências Exatas e Tecnologia, Universidade Federal do Pará,
Campus Universitário de Abaetetuba, 68440-000, Abaetetuba, Pará, Brazil*

With an intent to study the combined effect of Born-Infeld field as a nonlinear electrodynamics (BI-NED) and Perfect Fluid Dark Matter (PFDM) to Einstein- Λ theory of gravity, we obtain the exact charged AdS black hole solutions. Next, we study the effects of the parameters of PFDM and BI on the event horizon of these black holes. Then, we compute the conserved and thermodynamical quantities and evaluate that these thermodynamical quantities can satisfy the first law of thermodynamics. In addition, we investigate thermal stability conditions for these black hole solutions in context of canonical ensemble by using the heat capacity and the Helmholtz free energy. We study the effects of the parameters of PFDM and BI-NED on the local and global stability areas. Next, we extend our study to investigate thermodynamical properties of BI-NED AdS black holes surrounded by PFDM in extended phase space by considering the cosmological constant as a thermodynamics pressure. We, obtain the conserved and thermodynamic quantities which can satisfy the first law of thermodynamics in extended phase space. We then perform a rigorous analytical verification of the Ehrenfest equations to determine whether the critical behavior of the charged BI-NED AdS black holes surrounded by PFDM corresponds to a second-order phase transition. Our findings indicate that both Ehrenfest relations are satisfied, confirming that the black hole system undergoes a second-order phase transition at the critical point. we obtain heat engines corresponding to these black holes. The goal is to see how black holes' parameters such as parameters of PFDM and BI-NED would affect efficiency of the heat engines. Finally, we study the geodesic structure of the spacetime by analyzing both timelike and null geodesics. The effective potential is examined to determine the conditions for stable and unstable circular orbits, as well as the behavior of the innermost stable circular orbit and the photon sphere. We show that the PFDM parameter significantly modifies the orbital structure and potential barrier, while the Born-Infeld parameter produces comparatively weaker corrections. The existence of bound, critical, and unstable trajectories highlights the dynamical impact of dark matter and nonlinear electrodynamics on particle and photon motion around the black hole.

I. INTRODUCTION

A primary motivation for studying Nonlinear Electrodynamics (NED) stems from its inherent richness compared to the standard Maxwell theory; notably, NED encompasses the linear Maxwell field theory as a specific limiting case. Furthermore, theoretical shortcomings of the Maxwell field—such as its inability to adequately describe radiation within certain materials [1–3] and the challenge of modeling the self-interaction of virtual electron-positron pairs [4–6]—provide strong impetus for adopting NED formalisms [7].

Crucially, the incorporation of NED formalism offers a pathway to resolve the cosmological singularity at the Big Bang and the spacetime singularity associated with black holes [8–11]. Specifically, solutions for regular black holes within Einstein gravity can be derived when coupled to a suitable NED [8, 12–15]. Moreover, the influence of NED effects becomes profoundly significant in highly magnetized compact astrophysical objects, including neutron stars

*Electronic address: eslampanah@umz.ac.ir

†Electronic address: hamilbilel@gmail.com/bilel.hamil@umc.edu.dz

‡Electronic address: esialg@gmail.com

and pulsars [16–18]. Investigation into horizonless magnetic solutions resulting from various nonlinear electromagnetic fields has also been documented in the literature [19, 20]. A universal and noteworthy characteristic shared by all NED models is that solutions describing black holes coupled to these theories inherently satisfy both the zeroth and first laws of thermodynamics.

The inherent ultraviolet divergence associated with the electric field of a classical point charge at the origin necessitates the adoption of nonlinear extensions to Maxwell’s electrodynamics. To regularize this singularity, Born and Infeld proposed an influential formulation in 1934, known as Born-Infeld NED (BI-NED) [21, 22]. Subsequently, this framework was extended by Hoffmann through its coupling to General Relativity (GR) [23]. The resulting gravitational solutions coupled to BI-NED have been extensively explored across various theoretical domains. These investigations encompass the properties of static black hole metrics [24–26], the analysis of rotating compact objects [27, 28], the construction of wormhole geometries [29–32], and modeling phenomena within superconductors [33–35]. Moreover, the theoretical relevance of BI-NED has been significantly renewed by its natural emergence as the effective low-energy limit of open string theory [36–41].

A pivotal and enduring challenge in contemporary physics lies in the definitive elucidation of the nature of dark matter (DM). Despite its inferred contribution constituting approximately 27% of the universe’s total critical energy density, direct empirical detection remains unsuccessful, thereby cementing its status as one of the foremost unresolved enigmas within the domains of cosmology and high-energy particle physics. A comprehensive understanding of DM’s structural properties is indispensable, not solely for accurately characterizing the formation and evolutionary mechanisms of large-scale cosmic structures and galactic morphologies, but also for rigorously investigating its dynamic interplay with dark energy, the cosmological constant responsible for driving the observed accelerated expansion of the cosmos.

The Perfect Fluid Dark Matter (PFDM) model provides a compelling framework for investigating the role of DM in astrophysical and cosmological scenarios, particularly in relation to black holes. In contrast to standard particle-based models, the perfect fluid model conceptualizes DM as a continuous, non-viscous fluid governed by specific equations of state [42]. This fluid-like representation enables the rigorous modeling of DM distributions surrounding black holes and allows for an examination of how these distributions modify the observable characteristics of black hole spacetimes [43].

The introduction of PFDM model fundamentally modifies the spacetime geometries derived from GR. Extensive theoretical investigations have established that incorporating PFDM alters the characteristic metrics of established black hole solutions. Specifically, metric perturbations and their associated physical consequences have been rigorously predicted and analyzed for the vacuum Schwarzschild metric [44, 45], the charged Reissner-Nordström (RN) solution [46], the rotating Kerr metric [47, 48], the singularity-free Bardeen solution [49], and solutions derived from Euler-Heisenberg electrodynamics [50, 51]. These metric deformations carry significant physical ramifications, influencing observables such as gravitational wave signatures [52, 53], modifying geodesic motion [54], and altering the conditions for spacetime stability and thermodynamic phase transitions [55–57]. Furthermore, the presence of PFDM critically impacts several astrophysical signatures associated with black holes, including the analysis of gravitational lensing [58], the size and appearance of their shadows [59, 60], the characteristics of accretion disk structures [61], and the deflection angles of light [62].

The thermodynamic framework of black holes immersed in a PFDM background has been a focal point of study [63, 64], alongside investigations into their quasinormal modes [65, 66] and the calculation of their Gibbs free energy functions [67–69]. Moreover, both the structure of event horizons [70] and the viability of wormhole solutions [71] have demonstrated sensitivity to the PFDM background. More recently, specific studies have focused on complex configurations, for example; the thermodynamics and phase transitions of asymptotically ModMax anti-de Sitter (AdS) black holes under PFDM influence have been examined in Ref. [71], the impact of PFDM on particle dynamics surrounding a static black hole situated within an external magnetic field have been explored in Ref. [72]. Further investigations have characterized the phase structure and critical behavior of charged-AdS black holes [73], the photon orbits and phase transitions in Letelier AdS black holes [74], and the combined thermodynamics and geodesic structure [75] for these Letelier AdS solutions, all within the context of a PFDM background.

The investigation of black hole phase transitions utilizes methodologies from classical thermodynamics as well as the more modern field of thermodynamic geometry. In the classical framework, notable analogues include the relationship between charged AdS black holes and liquid-gas systems, along with the application of Ehrenfest relations. Banerjee et al. [77, 78] enhanced this approach by developing a novel formalism based on the Ehrenfest analogy between thermodynamic variables and black hole parameters ($V \leftrightarrow Q$, and $P \leftrightarrow -U$). Their analysis of black hole phase transitions treated these systems as grand-canonical ensembles and rigorously examined the Ehrenfest relations using both analytical and graphical techniques.

Among the recent thermodynamical advances in the field of black holes thermodynamics, one can point out to extended phase space and geometrical thermodynamics. In the extended phase space, one considers the cosmological constant in AdS black holes to be a thermodynamical quantity known as pressure [79–82]. Such consideration results

into introduction of a van der Waals behavior, the reentrant of phase transition [83, 84], existence of the triple point [85, 86] and possibility of having classical heat engine [87–105]. Furthermore, a new method for classification and analysis of the thermodynamic system was constructed based on topology [133]. In this method, topological invariant numbers are calculated, which, when summed, yield a global topological invariant that classifies the thermodynamics as exhibiting a predominance of stable states, unstable states, or an equilibrium between them. We shall employ this method to classify our new solution.

The investigation of geodesic motion around compact objects constitutes an essential tool for understanding the physical and geometrical properties of neutron stars and black holes. The trajectories of test particles encode valuable information about the underlying spacetime structure. A well-known observational example is provided by the motion of stars in the vicinity of Sagittarius A* at the center of the Milky Way galaxy [106, 107], which offers strong evidence for the presence of a supermassive black hole. In black hole spacetimes, radial and circular geodesics represent two fundamental classes of motion with direct astrophysical relevance. Consequently, geodesic dynamics in various gravitational backgrounds have been widely explored in the literature [108–116]. More generally, spacetime curvature effects can be systematically analyzed through the geodesic equation [117, 118], which governs the relative acceleration between neighboring geodesics under different physical conditions [119–121]. The geodesic equation therefore provides a powerful framework for characterizing spacetime geometry, and its solutions for timelike, null, and spacelike congruences yield important insights into gravitational dynamics.

These considerations motivate us to investigate topological AdS black holes in the presence of Born–Infeld nonlinear electrodynamics and perfect fluid dark matter. Our aim is to explore how the corresponding parameters, together with the topological constant, influence the properties of the black hole solutions. In particular, we examine their impact on the horizon structure, thermodynamic quantities, and phase behavior. Furthermore, by treating the black holes as heat engines, we analyze how these parameters affect the engine efficiency. Finally, we study the timelike and null geodesic structures to understand how nonlinear electrodynamics, and dark matter, modify particle and photon motion in the resulting spacetime.

II. ACTION AND FIELD EQUATIONS

The action of Einstein- Λ gravity in the presence of BI-NED field and DM is given by

$$\mathcal{I} = \int d^4x \sqrt{-g} \left[\left(\frac{R - 2\Lambda + \mathcal{L}(\mathcal{F})}{2\kappa^2} \right) + \mathcal{L}_{PFDM} \right], \quad (1)$$

where R is the Ricci scalar. Also, $\kappa^2 = 8\pi$ because we set $c = G = 1$ in the action (1), where c , and G , respectively, are the speed of light and the gravitational constant. In addition, \mathcal{L}_{PFDM} is the Lagrangian density of PFDM. In the above action, Λ is the cosmological constant, and g refers to the determinant of the metric tensor $g_{\mu\nu}$ (i.e., $g = \det(g_{\mu\nu})$). Furthermore, the term $\mathcal{L}(\mathcal{F})$ is related to the Lagrangian of BI-NED theory as

$$L(\mathcal{F}) = 4\beta^2 \left(1 - \sqrt{1 + \frac{\mathcal{F}}{2\beta^2}} \right), \quad (2)$$

in the above Lagrangian, β is the BI parameter. Also, \mathcal{F} is the Maxwell invariant in the form $\mathcal{F} = F_{\mu\nu}F^{\mu\nu}$, in which $F_{\mu\nu}$ is the electromagnetic field tensor and is defined as $F_{\mu\nu} = \partial_\mu A_\nu - \partial_\nu A_\mu$, where A_μ is the gauge potential.

Now, we are in a position to obtain field equations. Applying variational principle to the action (1), one can find

$$G_\mu^\nu - \frac{1}{2}g_\mu^\nu L(\mathcal{F}) + 2L_{\mathcal{F}}F_{\mu\sigma}F^{\sigma\nu} = 8\pi T_\mu^\nu, \quad (3)$$

$$\nabla_\mu (\sqrt{-g}L_{\mathcal{F}}F^{\mu\nu}) = 0, \quad (4)$$

where $L_{\mathcal{F}} = \frac{dL(\mathcal{F})}{d\mathcal{F}}$ and $G_\mu^\nu = R_\mu^\nu - \frac{1}{2}g_\mu^\nu R$.

In Eq. (3), T_μ^ν is the energy momentum tensor of PFDM, and it can be expressed in the following form

$$T_\mu^\nu = \begin{pmatrix} -\rho & 0 & 0 & 0 \\ 0 & p_r & 0 & 0 \\ 0 & 0 & p_\theta & 0 \\ 0 & 0 & 0 & p_\varphi \end{pmatrix} = \begin{pmatrix} \frac{b}{8\pi r^3} & 0 & 0 & 0 \\ 0 & \frac{b}{8\pi r^3} & 0 & 0 \\ 0 & 0 & \frac{-b}{16\pi r^3} & 0 \\ 0 & 0 & 0 & \frac{-b}{16\pi r^3} \end{pmatrix}, \quad (5)$$

We consider a static spherical symmetric in 4-dimensional spacetime in the following form

$$ds^2 = -\psi(r) dt^2 + \frac{dr^2}{\psi(r)} + r^2(d\theta^2 + \sin^2\theta d\varphi^2), \quad (6)$$

where $\psi(r)$ is the metric function.

Now, we consider a radial electric field which its related gauge potential is

$$A_\mu = h(r) \delta_\mu^t, \quad (7)$$

Using Eqs. (4), (6) and (7), we obtain following differential equations

$$r\beta^2 H'(r) - 2H^3(r) + 2\beta^2 H(r) = 0, \quad (8)$$

where $H(r) = h'(r) = \frac{dh(r)}{dr}$, and prime denotes derivation with respect to radial coordinate. It is a matter of calculation to show that

$$H(r) = \frac{q}{r^2\Gamma}, \quad (9)$$

where $\Gamma = \sqrt{1 + \frac{q^2}{\beta^2 r^4}}$ and q is an integration constant related to the electric charge.

By employing Eqs. (6), and (9) within Eq. (3), we can find the components of the equations of motion (Eq. (3)), which are

$$eq_{tt} = \psi(r) + r\psi'(r) - \frac{2\beta^2 r^3 + r + b}{r} + \frac{2\beta^2 r^2}{\Delta}, \quad (10)$$

$$eq_{\theta\theta} = r\psi'(r) + \frac{r^2\psi''(r)}{2} - 2\beta^2 r^2(1 - \Delta) + \frac{b}{2r}, \quad (11)$$

where $\Delta = \sqrt{1 - \left(\frac{H(r)}{\beta}\right)^2}$. In addition, $eq_{tt} = eq_{rr}$, and $eq_{\theta\theta} = eq_{\varphi\varphi}$, where eq_{tt} , eq_{rr} , $eq_{\theta\theta}$ and $eq_{\varphi\varphi}$ are related to components of tt , rr , $\theta\theta$ and $\varphi\varphi$ of the equations of motion (Eq. (3)).

III. BLACK HOLE SOLUTIONS

By considering equations of motion (Eqs. (10) and (11)), we can obtain the metric function $\psi(r)$ in the following form

$$\psi(r) = 1 - \frac{2m_0}{r} - \frac{\Lambda r^2}{3} + \frac{2\beta^2 r^2(1 - \mathfrak{F}_1)}{3} + \frac{b}{r} \ln\left(\frac{r}{|b|}\right), \quad (12)$$

where $\mathfrak{F}_1 = {}_2F_1\left(\left[\frac{-1}{2}, \frac{-3}{4}\right], \left[\frac{1}{4}\right], 1 - \Gamma^2\right)$ is the hypergeometric function. Also m_0 is an integration constant related to geometrical mass of the solution.

It is notable that the obtained solutions in Eq. (12) reduce to the charged AdS black hole solutions in the presence of PFDM when $\beta \rightarrow \infty$, i.e.,

$$\psi(r) = 1 - \frac{2m_0}{r} - \frac{\Lambda r^2}{3} + \frac{q}{r^2} + \frac{b}{r} \ln\left(\frac{r}{|b|}\right). \quad (13)$$

In addition, by considering $\beta \rightarrow \infty$, and $b = 0$, the metric function $\psi(r)$ (Eq. (12)) turns to the charged AdS black hole solutions in the following form

$$\psi(r) = 1 - \frac{2m_0}{r} - \frac{\Lambda r^2}{3} + \frac{q}{r^2}. \quad (14)$$

Our next step is to examine the geometrical structure of the solutions. First, we will investigate the existence of essential singularities. For this purpose, we calculate the Ricci and Kretschmann scalars of these spacetimes.

We can get the Ricci scalar (R) of the solutions in the following form

$$R = 4\Lambda - 8\beta^2(1 - \mathfrak{F}_1) - \frac{b}{r^3} + \frac{12q^2\mathfrak{F}_2}{r^4} + \frac{8q^4\mathfrak{F}_3}{5\beta^2 r^8}, \quad (15)$$

where \mathfrak{F}_2 , and \mathfrak{F}_3 defined as

$$\begin{aligned}\mathfrak{F}_2 &= {}_2F_1\left(\left[\frac{1}{2}, \frac{1}{4}\right], \left[\frac{5}{4}\right], 1 - \Gamma^2\right), \\ \mathfrak{F}_3 &= {}_2F_1\left(\left[\frac{3}{2}, \frac{5}{4}\right], \left[\frac{9}{4}\right], 1 - \Gamma^2\right).\end{aligned}\quad (16)$$

The Kretschmann scalar ($K = R_{\mu\nu\rho\sigma}R^{\mu\nu\rho\sigma}$) of this spacetime is

$$\begin{aligned}K &= \frac{32\left(\beta^2(\mathfrak{F}_1 - 1) + \frac{\Lambda}{2}\right)\left(\beta^2(\mathfrak{F}_1 - 1) + \frac{2\Lambda r^3 - b}{4r^3}\right)}{3} + \frac{32q^2\beta^2\mathfrak{F}_2(\mathfrak{F}_1 - 1) + 4(1 + 4\Lambda q^2\mathfrak{F}_2) - 4}{r^4} \\ &+ \frac{8m_0(5b - 6\mathcal{B}_{1,0,1})}{r^6} + \frac{\left(12\ln^2\left(\frac{r}{|b|}\right) - 20\ln\left(\frac{r}{|b|}\right) + 13\right)b^2}{r^6} + \frac{8q^2\mathfrak{F}_2\mathcal{B}_{6,7,12}}{r^7} \\ &+ \frac{16q^4\left(75\mathfrak{F}_2^2 + 4\mathfrak{F}_3\left(\mathfrak{F}_1 - 1 + \frac{\Lambda}{2\beta^2}\right)\right)}{15r^8} - \frac{16q^4\mathfrak{F}_3\mathcal{B}_{2,3,4}}{5\beta^2r^{11}} - \frac{64q^6\mathfrak{F}_2\mathfrak{F}_3}{5\beta^2r^{12}} + \frac{64q^8\mathfrak{F}_3^2}{25\beta^4r^{16}},\end{aligned}\quad (17)$$

where $\mathcal{B}_{i,j,k} = ib \ln\left(\frac{r}{|b|}\right) - jb - km_0$. Whereas these scalar diverge at $r = 0$, i.e.,

$$\begin{aligned}\lim_{r \rightarrow 0} R &\rightarrow \infty, \\ \lim_{r \rightarrow 0} R_{\mu\nu\rho\sigma}R^{\mu\nu\rho\sigma} &\rightarrow \infty,\end{aligned}\quad (18)$$

so there is an essential curvature singularity at $r = 0$.

On the other hand, the asymptotical behavior of these solutions is (A)dS, because

$$\begin{aligned}\lim_{r \rightarrow \infty} R &\rightarrow 4\Lambda, \\ \lim_{r \rightarrow \infty} R_{\mu\nu\rho\sigma}R^{\mu\nu\rho\sigma} &\rightarrow \frac{8\Lambda^2}{3},\end{aligned}\quad (19)$$

Our analysis indicate that there is an essential curvature singularity at $r = 0$. To understand that the singularity covered by an event horizon, we plot the metric function $\psi(r)$ versus r in two panels in Figure. 1. As one can see, the singularity is covered by an event horizon. So, the obtained solutions are black hole solution. In addition, we study the effects of the parameters of PFDM (b) and BI-NED (β) on the root of metric function ($\psi(r)$). Our findings reveal that there are three different behaviors for root of BI-NED AdS black holes where only depend on the parameters b and β . Indeed, by varying b and β the number of roots of the metric function change when other parameters are fixed. These behaviors are:

i) For small values of b , there are two roots. The small root is related to the inner horizon and the large root is the event horizon. Such behavior of the metric function was reported for Rissner-Nordestron (RN) black holes (see dashed line in the left panel of Fig. 1 (Fig. 1a)). However, for small values of β , there is only one root and it is related to the event horizon ((see dashed and dashed-dotted lines in the right panel of Fig. 1 (Fig. 1b)))

ii) For medium values of b and β , there are three roots. In other words, we encounter with multi-horizons black holes (two inner horizons and one event horizon), see dashed-dotted and continuous lines in the left panel of Fig. 1 (Fig. 1a) and continuous line in the right panel of Fig. 1 (Fig. 1b).

iii) For large values of b , there is only one root and it is related to the event horizon. This black holes behaves similar to the Schwarzschild black holes (see the dotted line in the left panel of Fig. 1 (Fig. 1a)). However, for large value of β , there are two roots. The small root is related to the inner horizon and the large root is the event horizon. Such behavior of the metric function was reported for Rissner-Nordestron (RN) black holes (see the dotted line in the right panel of Fig. 1 (Fig. 1b)).

There are two distinct behaviors observed when varying the parameters of PFDM (b) and BI-NED (β):

i) Number of Roots: The number of roots of the metric function first increases from two to three as the PFDM parameter increases, then decreases from three to one (see the left panel in Fig. 1). In contrast, when varying the

BI parameter, the number of roots of $f(r)$ increases from one to three and then decreases to two as the value of β increases (see the right panel in Fig. 1).

ii) **Event Horizon:** Increasing the PFDM parameter results in an increase in the event horizon (or black hole size), see the left panel in Fig. 1, for more details. Conversely, increasing the BI-NED parameter leads to a decrease in the event horizon (see the right panel in Fig. 1).

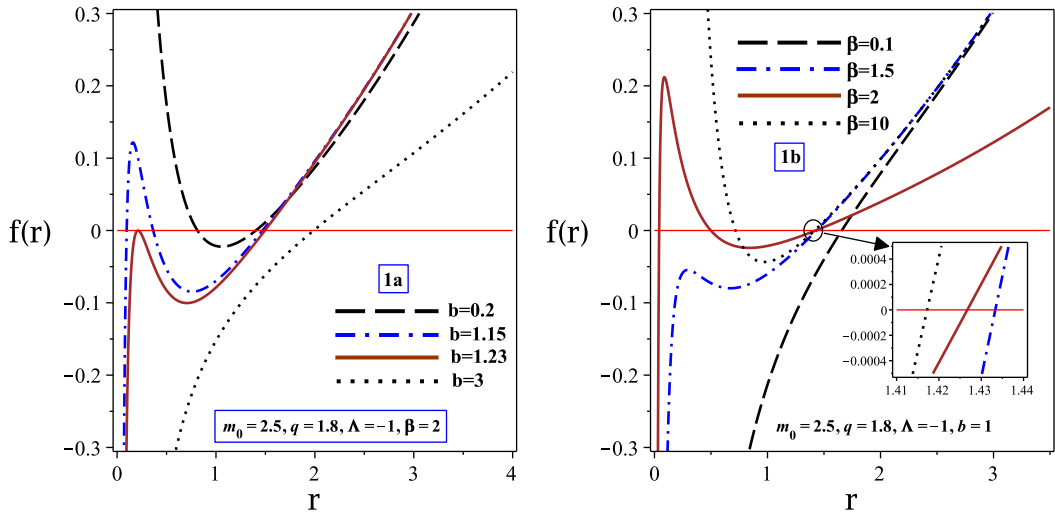


FIG. 1: The metric function $\psi(r)$ versus r for different values of parameters b in the left panel, and β in the right panel.

IV. THERMODYNAMIC PROPERTIES IN NON-EXTENDED PHASE SPACE

Considering BI-NED AdS black holes surrounded by PFDM, we calculate the conserved and thermodynamical quantities such as Hawking temperature, entropy, charge, electric potential, and total mass. Then we evaluate the effect of PFDM parameters on these quantities. Using these thermodynamical quantities, we check that these quantities satisfy the first law of thermodynamics. Then, we are going to expand our study to local and global stability conditions of the solutions in canonical ensemble by studying the heat capacity and the Helmholtz free energy, respectively.

A. Conserved and Thermodynamic Quantities

Due to the fact that employed metric only contains one temporal killing vector ($\chi_\mu = (1, 0, 0, 0)$), one can use the concept of surface gravity ($\kappa = \sqrt{\nabla_\mu \chi_\nu \nabla^\mu \chi^\nu}$) for calculating the temperature on the event horizon (r_+) which leads to

$$T = \frac{\kappa}{2\pi} = \frac{1}{2\pi} \sqrt{\nabla_\mu \chi_\nu \nabla^\mu \chi^\nu} = \frac{1}{4\pi} \frac{d\psi(r)}{dr} \Big|_{r=r_+}, \quad (20)$$

by considering Eqs. (12) and (20), we can get the Hawking temperature for these black holes as

$$T = \frac{\left(1 + \frac{b}{r_+}\right)}{4\pi r_+} + \frac{(2\beta^2 (1 - \mathfrak{F}_{1+}) - \Lambda) r_+}{4\pi} - \frac{q^2 \mathfrak{F}_{2+}}{\pi r_+^3}, \quad (21)$$

where $\mathfrak{F}_{1+} = \mathfrak{F}_1|_{r=r_+}$, $\mathfrak{F}_{2+} = {}_2F_1\left(\left[\frac{1}{2}, \frac{1}{4}\right], \left[\frac{5}{4}\right], 1 - \Gamma_+^2\right)$, and $\Gamma_+ = \Gamma|_{r=r_+}$. It is clear that the parameters of PFDM and BI-NED influence the Hawking temperature of these black holes.

The entropy of these black holes can be obtained by using the area law, in the following form

$$S = \frac{A}{4}, \quad (22)$$

where A is the horizon area and is obtained

$$A = \int_0^{2\pi} \int_0^\pi \sqrt{g_{\theta\theta}g_{\varphi\varphi}} \Big|_{r=r_+} = 4\pi r^2 \Big|_{r=r_+} = 4\pi r_+^2, \quad (23)$$

so the entropy of BI-NED AdS black holes surrounded by PFDM is given by

$$S = \pi r_+^2. \quad (24)$$

We can get the electric charge of the solutions by employ the Gauss law in the following form

$$Q = \frac{F_{tr}}{4\pi} \int_0^{2\pi} \int_0^\pi \sqrt{g} d\theta d\varphi = q, \quad (25)$$

where for case $t = \text{constant}$ and $r = \text{constant}$, the determinant of metric tensor g is $r^4 \sin^2 \theta$.

In order to obtain electric potential, we can calculate it on the horizon with respect to a reference which leads to

$$\Phi = A_\mu \chi^\mu \Big|_{r \rightarrow \infty} - A_\mu \chi^\mu \Big|_{r \rightarrow r_+} = \frac{q}{r_+} \mathfrak{F}_{2+}, \quad (26)$$

Applying Ashtekar-Magnon-Das (AMD) approach, we find the total mass of these black holes in the following form

$$M = m_0, \quad (27)$$

where m_0 is the geometrical mass and is given by solving $(\psi(r = r_+) = 0)$. So the total mass is given by

$$M = \frac{r_+ + b \ln\left(\frac{r_+}{|b|}\right)}{2} + \left(\frac{\beta^2 (1 - \mathfrak{F}_{1+})}{3} - \frac{\Lambda}{6}\right) r_+^3. \quad (28)$$

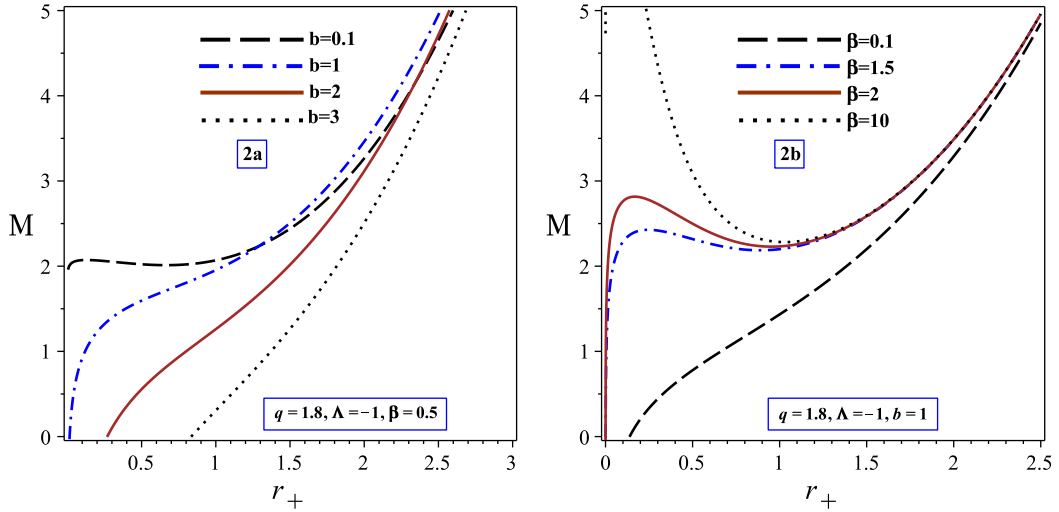


FIG. 2: The total mass M versus r_+ for different values of b (the left panel) and β (the right panel).

Now, we can examine the effect of the parameters of PFDM and BI-NED on total mass. For this purpose, we series M versus q up to order (q^6) which leads to

$$M \simeq \frac{r_+}{2} + \frac{b \ln\left(\frac{r_+}{|b|}\right)}{2} - \frac{\Lambda r_+^3}{6} + \frac{q^2}{2r_+} - \frac{q^4}{40\beta^2 r_+^5} + \frac{q^6}{144\beta^4 r_+^9}. \quad (29)$$

Our findings indicate that the asymptotically behavior of M is the same for various values of b , q and β because the asymptotical behavior of M depends on the cosmological constant ($\lim_{r \rightarrow \infty} M \propto \frac{-\Lambda r_+^3}{6}$). So, for the negative of the cosmological constant, the total mass increases by increasing the size of black hole (or r_+).

High-energy limit of M in the absence of the electric charge only depends on the PFDM's parameter as $\lim_{r \rightarrow 0} M \propto \frac{b \ln\left(\frac{r_+}{|b|}\right)}{2}$. In the presence of q , and for small value of b , the total mass is the finite positive at $r \rightarrow 0$ (except $r = 0$), see the dashed line in the left panel of Fig. 2 (Fig. 2a). For medium value of b , $\lim_{r \rightarrow 0} M \rightarrow 0$, see the dashed-dotted line in the left panel of Fig. 2 (Fig. 2a). For large value of b , there are black holes with $M = 0$ at finite radius (see continuous and dotted lines in the left panel of Fig. 2 (Fig. 2a)). It is notable that the finite radius shifts to large radius when b increases. Our analysis indicate that the behavior of mass of the small black holes is very sensitive to the parameter of PFDM (b). Such behaviors are different of usual black holes such as Schwarzschild and Reissner-Nordström black holes.

On the other hand, the effect of BI-NED parameter on the total mass is different of PFDM's parameter. In other words, by decreasing of values of β , the divergence of total mass removes and it reach to a finite value (see the right panel in Fig. 2 (Fig. 2b)). In addition, for very large values of β , at $r_+ = 0$, the total mass behaves similar to Reissner-Nordström black holes because $\lim_{r \rightarrow 0} M \rightarrow \infty$.

As a result, the divergence of total mass (at $r_+ = 0$) of BI-NED AdS black holes surrounded by PFDM removes when the parameter of BI-NED decreases or the parameter of PFDM includes large value. In other words, the effects of these parameters on the total mass act opposite each other.

Replacing Eqs. (24) and (25) within Eq. (28), we can obtain $M = M(S, Q)$ in the following form

$$M(S, Q) = \left(\frac{1}{2} - \frac{\Lambda S}{6\pi} + \frac{S(1 - \mathfrak{F}_{1SQ})\beta^2}{3\pi} + \frac{b\sqrt{\pi} \ln\left(\frac{\sqrt{S}}{|b|\sqrt{\pi}}\right)}{2\sqrt{S}} \right) \sqrt{\frac{S}{\pi}}, \quad (30)$$

where $\mathfrak{F}_{1SQ} = {}_2F_1\left(\left[\frac{-1}{2}, \frac{-3}{4}\right], \left[\frac{1}{4}\right], -\frac{\pi^2 Q^2}{\beta^2 S^2}\right)$.

Now, we are in a position to study the first law of thermodynamics. Here, we should calculate $\left(\frac{\partial M}{\partial S}\right)_Q$ and $\left(\frac{\partial M}{\partial Q}\right)_S$, and then use Eqs. (24) and (25) to convert them as functions of r_+ and q . After some simplifications, one finds that these quantities are, respectively, the same as temperature ($T = \left(\frac{\partial M}{\partial S}\right)_Q$) and electric potential ($\Phi = \left(\frac{\partial M}{\partial Q}\right)_S$) which were obtained in Eqs. (21) and (26). Hence, although the parameters of PFDM and BI-NED affected thermodynamic and conserved quantities, the first law remains valid as

$$dM = TdS + \Phi dQ. \quad (31)$$

B. Heat Capacity: Local Stability

In the context of canonical ensemble, thermal stability (or local stability) conditions of topological BI-NED AdS black holes surrounded by PFDM determine by the sign of heat capacity. The positivity of heat capacity guarantees thermally stable solutions, whereas the negative heat capacity is denoted as an unstable state. On the other hand, positive and negative of the temperature determine the physical and non-physics thermal system. So, we study the sign of heat capacity and temperature to obtain physical and stable areas.

The heat capacity is defined as

$$C = T \left(\frac{\partial S}{\partial T} \right)_Q = T \frac{\left(\frac{\partial S}{\partial r_+} \right)_Q}{\left(\frac{\partial T}{\partial r_+} \right)_Q}. \quad (32)$$

Using obtained temperature (Eq. (21)) and entropy (24), we can obtain the heat capacity in the following form

$$C = \frac{\pi \left(\mathfrak{F}_{1+} + 2(\Gamma_+^2 - 1)\mathfrak{F}_{2+} - \frac{(2\beta^2 - \Lambda)r_+^3 + b + r_+}{2\beta^2 r_+^3} \right) r_+^2}{\mathfrak{F}_{1+} + \frac{4(\Gamma_+^2 - 1)^2 \mathfrak{F}_{3+}}{5} - \frac{(2\beta^2 - \Lambda)r_+^3 - 2b - r_+}{2\beta^2 r_+^3}}, \quad (33)$$

in which where $\mathfrak{F}_{3+} = \mathfrak{F}_3|_{r=r_+}$.

Now, we examine the local thermodynamic stability by plotting the heat capacity (Eq. (33)) and temperature (Eq. (21)) as functions of the event horizon radius r_+ . To this end, two panels are presented in Fig. 3 to analyze the influence of the parameters of PFDM and BI-NED on the stability regions. Our results reveal that:

- The effect of the PFDM parameter is illustrated in the left panel of Fig. 3 (Fig. 3a). Our findings indicate that: i) There is a critical value for b , at which we can find two roots (the first root is denoted as r_{0_1} and the second root as r_{0_2}) and one divergence point (denoted as r_{+div}) for the heat capacity when $b < b_{critical}$ (see the dashed line in the left panel of Fig. 3). Notably, the divergence point is located between the two roots, i.e., $r_{0_1} < r_{+div} < r_{0_2}$. Both the heat capacity and temperature are positive when $r_+ > r_{0_2}$, indicating that large black holes can satisfy the local stability condition. ii) For $b > b_{critical}$, as b increases, there is only one divergence point in the heat capacity. As the PFDM parameter increases, this divergence point shifts toward larger horizon radii. In this scenario, the heat capacity is negative for $r_+ < r_{+div}$ and becomes positive for $r_+ > r_{+div}$. Thus, the BI-NED AdS black holes surrounded by PFDM satisfy the local thermodynamic stability condition, as both C and T are positive when $r_+ > r_{+div}$. Additionally, the local stability area decreases as b increases.
- Considering the different values for the BI-NED parameter, the heat capacity and temperature of these black holes are plotted in the right panel of Fig. 3 (Fig. 3b). i) There is a critical value for the BI-NED parameter at which the heat capacity exhibits two roots and one divergence point when $\beta > \beta_{critical}$ (see the continuous and dashed-dotted lines in the right panel of Fig. 3). The heat capacity and temperature are simultaneously positive when $r_+ > r_{0_2}$. Indeed, the local stability area is located in the range $r_+ > r_{0_2}$. ii) For $\beta < \beta_{critical}$, there is only one divergence point where C and T are positive when $r_+ > r_{+div}$, and they become negative when $r_+ < r_{+div}$. In other words, large BI-NED AdS black holes can satisfy the local stability conditions. Conversely, as β increases, the local stability area initially increases and then decreases.

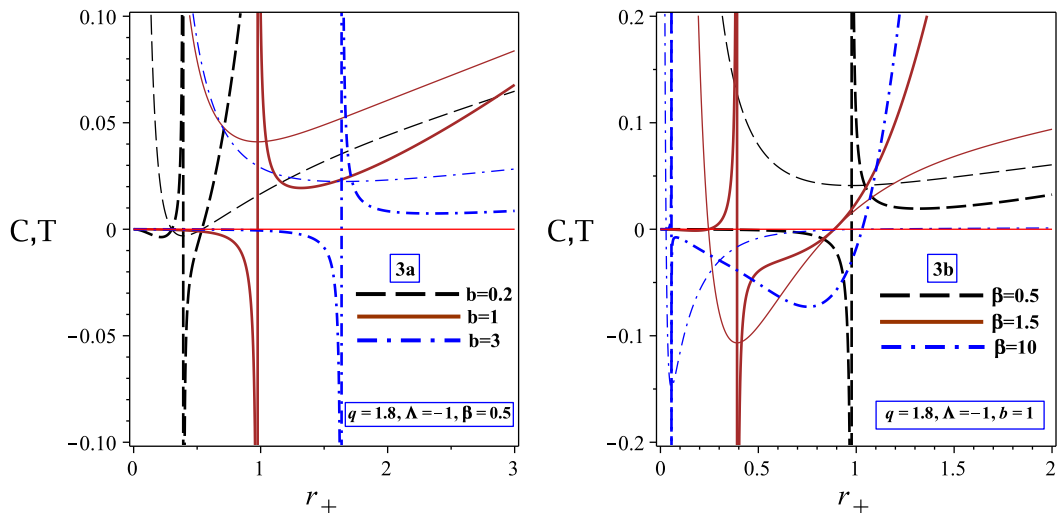


FIG. 3: The heat capacity C (thick lines) and temperature T (thin lines) are shown as functions of r_+ for different values of b in the left panel and β in the right panel.

C. Helmholtz free energy: Global Stability

In the canonical ensemble context, the negative of Helmholtz free energy (F) determines the global stability. So, we employ the Helmholtz free energies to evaluate the global stability of the BI-NED AdS black holes surrounded by PFDM.

While the conventional thermodynamic definition for the Helmholtz free energy is given by $F = U - TS$, it is crucial to note that within the context of black hole thermodynamics, this potential is redefined as follows

$$F = M - TS, \quad (34)$$

by applying Eqs. (21), (24) and (28) within Eq. (34), we find the Helmholtz free energy of these black holes in the following form

$$F = \frac{\left(\mathfrak{F}_{1+} + 6(\Gamma_+^2 - 1)\mathfrak{F}_{2+} + \frac{6b \ln(\frac{r_+}{|b|}) + 3(r_+ - b) + \Lambda r_+^3}{2\beta^2 r_+^3} - 1 \right) \beta^2 r_+^3}{6}, \quad (35)$$

where it depends on all the system parameters, especially those of PFDM and BI-NED.

Now, we can evaluate the global stability condition by study the Helmholtz free energy. As we mentioned, in the canonical ensemble context, black holes satisfy the global stability condition when F is negative (i.e., $F < 0$). Due to complexity of the Helmholtz free energy, we plot F versus r_+ by varying the parameters of PFDM and BI-NED when the other parameters are fixed in Fig. 4. Our analysis indicate that

- The effect of the PFDM parameter on F and T is plotted in the left panel of Fig. 4 (Fig. 4a). We find that: i) There is a critical value of the PFDM parameter. For $b < b_{critical}$, two roots for F appear; before the first root and after the second root, the Helmholtz free energy is negative, while it is positive between these roots (see the continuous line in the left panel of Fig. 4). This indicates that both small and large BI-NED AdS black holes can satisfy the global stability condition. ii) For $b > b_{critical}$, the black holes satisfy the global stability condition at every radius (see the dashed-dotted line in the panel of Fig. 4). iii) For very large values of $b \ll b_{critical}$, only large black holes can satisfy the condition $F < 0$ (see the dashed line in the left panel of Fig. 4).
- The variation of β with respect to heat capacity and temperature versus the event horizon (r_+) is illustrated in the right panel of Fig. 4 (Fig. 4b). Our findings reveal the following: i) Increasing β results in a decrease in the global stability area. ii) There are two roots where the Helmholtz free energy is positive between these roots. Therefore, medium black holes (i.e., those in the range $r_{01} < r_+ < r_{02}$) cannot satisfy the global stability conditions because F is positive in this region. iii) As $\beta \rightarrow \infty$, there is one root where F is positive before this root and negative afterward. In other words, large BI-NED AdS black holes can satisfy the global stability conditions when $\beta \rightarrow \infty$.

V. THERMODYNAMIC PROPERTIES IN EXTENDED PHASE SPACE

Here, we extend our study by considering the cosmological constant as a thermodynamics pressure. Indeed, in the extended phase space, the cosmological constant acts as a thermodynamic variable corresponding to pressure [79–82] in the following form

$$P = \frac{-\Lambda}{8\pi}, \quad (36)$$

where this postulate leads to an interpretation of the black hole mass as enthalpy [79].

By substituting $\Lambda = -8\pi P$ within the equation (30), we find

$$M(S, Q, P, b) = \left(\frac{1}{2} + \frac{4PS}{3} + \frac{S(1 - \mathfrak{F}_{1SQ})\beta^2}{3\pi} + \frac{b\sqrt{\pi} \ln\left(\frac{\sqrt{S}}{|b|\sqrt{\pi}}\right)}{2\sqrt{S}} \right) \sqrt{\frac{S}{\pi}}. \quad (37)$$

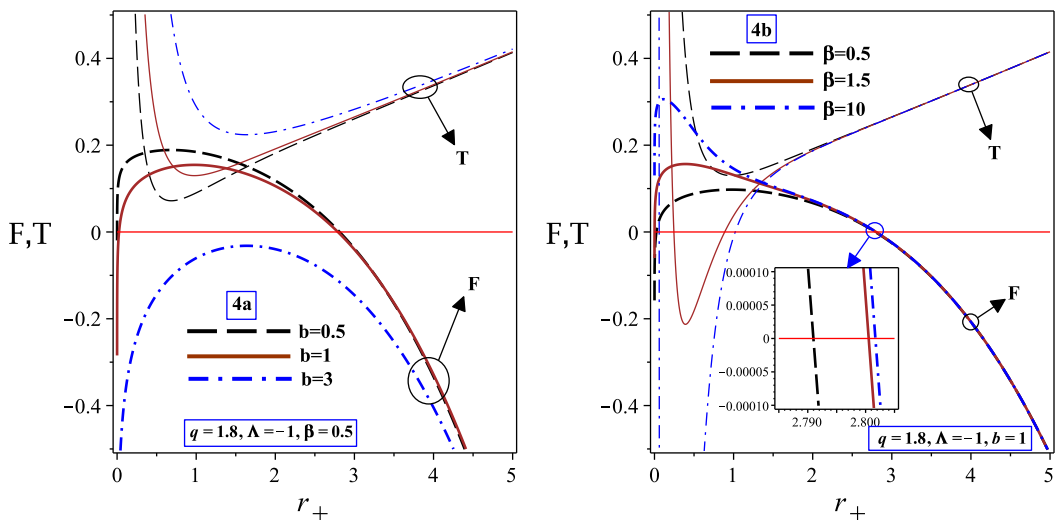


FIG. 4: The metric function $\psi(r)$ versus r for different parameters b in the left panel and β in the right panel.

Using Eq. (37), we can the conjugate quantities associated with the intensive parameters S , Q , P , and b , which are

$$T = \left(\frac{\partial M(S, Q, P, b)}{\partial S} \right)_{Q, P, b} = \frac{(\beta^2 (1 - \mathfrak{F}_{1SQ}) + 4\pi P) \sqrt{\frac{S}{\pi}} + b + 2\sqrt{\frac{S}{\pi}}}{2\pi} - \frac{Q^2 \mathfrak{F}_{2SQ} \sqrt{\frac{\pi}{S}}}{S}, \quad (38)$$

$$V = \left(\frac{\partial M(S, Q, P, b)}{\partial P} \right)_{S, Q, b} = \frac{4S^{3/2}}{3\pi^{1/2}}, \quad (39)$$

$$\Phi = \left(\frac{\partial M(S, Q, P, b)}{\partial Q} \right)_{S, P, b} = \frac{\sqrt{\pi} Q \mathfrak{F}_{2SQ}}{\sqrt{S}}, \quad (40)$$

$$B = \left(\frac{\partial M(S, Q, P, b)}{\partial b} \right)_{S, Q, P} = \frac{\ln\left(\frac{\sqrt{S}}{|b|\sqrt{\pi}}\right) - 1}{2}, \quad (41)$$

where $\mathfrak{F}_{2SQ} = {}_2F_1\left(\left[\frac{1}{2}, \frac{1}{4}\right], \left[\frac{5}{4}\right], -\frac{\pi^2 Q^2}{\beta^2 S^2}\right)$. Also, the conserved and thermodynamic quantities (Eqs. (37)-(41)) satisfy the first law of thermodynamics in extended phase space as

$$dM = TdS + \Phi dQ + VdP + Bdb. \quad (42)$$

In Refs. [122, 123], it was suggested that there is a link between super-entropy black holes and thermodynamic instability. Cofirming this connection would be of great importance. It should be mentioned that super-entropy black holes are a result of the violation of the inverse isoperimetric inequality [124]. Indeed, a black hole can be a super-entropy black hole if it meets the condition $\mathcal{R} < 1$, otherwise, it cannot be a super-entropy black hole. It is notable that \mathcal{R} defined as the isoperimetric ratio in the following form [124]

$$\mathcal{R} = \left(\frac{3V}{\mathcal{V}}\right)^{1/3} \left(\frac{\mathcal{V}}{A}\right)^{1/2}, \quad (43)$$

where $\mathcal{V} = 4\pi$ for the static spherical symmetric in 4-dimensional spacetime. By replacing Eqs. (23), and (39) within the above relation, we find that

$$\mathcal{R} = 1, \quad (44)$$

so these black holes cannot be super-entropy black holes, however the reverse isoperimetric inequality ($\mathcal{R} \geq 1$) can be satisfied [124].

A. Classical Ehrenfest Relations

In classical thermodynamics, phase transitions are classified as either first-order or higher-order transitions using the Clausius-Clapeyron and Ehrenfest equations. A first-order transition satisfies the Clausius-Clapeyron equation, while a second-order transition follows the Ehrenfest relations.

Banerjee et al. [125] presented a compelling analogy of the Ehrenfest equations by comparing thermodynamic state variables—specifically, $V \leftrightarrow Q$ and $P \leftrightarrow -\Phi$ —with black hole parameters. This comparison leads to

$$-\left(\frac{\partial\Phi}{\partial T}\right)_S = \frac{C_{\Phi_2} - C_{\Phi_1}}{TQ(\alpha_2 - \alpha_1)} = \frac{\Delta C_\Phi}{TQ\Delta\alpha}, \quad (45)$$

$$-\left(\frac{\partial\Phi}{\partial T}\right)_Q = \frac{\alpha_2 - \alpha_1}{\kappa_{T_2} - \kappa_{T_1}} = \frac{\Delta\alpha}{\Delta\kappa_T}, \quad (46)$$

where Φ is the electric potential. Also, V is the thermodynamic volume of the black hole. In addition, α and κ_T are the analogs of the volume expansion coefficient and the isothermal compressibility, respectively, and are defined as

$$\alpha = \frac{1}{Q} \left(\frac{\partial Q}{\partial T}\right)_\Phi, \quad (47)$$

$$\kappa_T = \frac{1}{Q} \left(\frac{\partial Q}{\partial\Phi}\right)_T. \quad (48)$$

The established link between $P - V$ criticality and the specific heat of black holes at constant pressure (C_P) allows for the direct application of the classical Ehrenfest equations in black hole research. Therefore, in this section, we will analytically verify the following Ehrenfest equations

$$\left(\frac{\partial P}{\partial T}\right)_S = \frac{C_{P_2} - C_{P_1}}{VT(\alpha_2 - \alpha_1)} = \frac{\Delta C_P}{VT\Delta\alpha}, \quad (49)$$

$$\left(\frac{\partial P}{\partial T}\right)_V = \frac{\alpha_2 - \alpha_1}{\kappa_{T_2} - \kappa_{T_1}} = \frac{\Delta\alpha}{\Delta\kappa_T}, \quad (50)$$

where α and κ_T are given by [126]

$$\alpha = \frac{1}{V} \left(\frac{\partial V}{\partial T}\right)_P, \quad (51)$$

$$\kappa_T = \frac{-1}{V} \left(\frac{\partial V}{\partial P}\right)_T. \quad (52)$$

We will calculate the relevant quantities in equations (49)-(50) to analyze the $P - V$ criticality in the extended phase space of BI-NED AdS black holes surrounded by PFDm.

Using Eq. (37), the specific heat of black holes at constant pressure (C_P) is obtained as

$$C_P = T \left(\frac{\partial S}{\partial T}\right)_P = \frac{2 \left(\mathfrak{F}_{1SQ} + \frac{2\pi^2 Q^2}{\beta^2 S^2} \mathfrak{F}_{2SQ} - \frac{(b + \sqrt{\frac{S}{\pi}})\pi^{3/2}}{2\beta^2 S^{3/2}} - \frac{4\pi P}{\beta^2} - 1 \right) S}{\mathfrak{F}_{1SQ} + \frac{4\pi^4 Q^4}{5\beta^4 S^4} \mathfrak{F}_{3SQ} + \frac{(2b + \sqrt{\frac{S}{\pi}})\pi^{3/2}}{2\beta^2 S^{3/2}} - \frac{4\pi P}{\beta^2} - 1}. \quad (53)$$

where \mathfrak{F}_{3SQ} is defined as

$$\mathfrak{F}_{3SQ} = {}_2F_1 \left(\left[\frac{3}{2}, \frac{5}{4} \right], \left[\frac{9}{4} \right], -\frac{\pi^2 Q^2}{\beta^2 S^2} \right).$$

We can obtain the volume expansion coefficient and the isothermal compressibility coefficient by applying Eqs. (38)

and (39) in conjunction with Eqs. (51) and (52). This results in

$$\alpha = \frac{1}{V} \left(\frac{\partial V}{\partial T} \right)_P = \frac{-6\pi^{3/2}}{\beta^2 S^{1/2} \left(\mathfrak{F}_{1SQ} + \frac{4\pi^4 Q^4}{5\beta^4 S^4} \mathfrak{F}_{3SQ} + \frac{(2b + \sqrt{\frac{S}{\pi}})\pi^{3/2}}{2\beta^2 S^{3/2}} - \frac{4\pi P}{\beta^2} - 1 \right)}, \quad (54)$$

$$\kappa_T = \frac{-1}{V} \left(\frac{\partial V}{\partial P} \right)_T = \frac{-12\pi}{\beta^2 \left(\mathfrak{F}_{1SQ} + \frac{4\pi^4 Q^4}{5\beta^4 S^4} \mathfrak{F}_{3SQ} + \frac{(2b + \sqrt{\frac{S}{\pi}})\pi^{3/2}}{2\beta^2 S^{3/2}} - \frac{4\pi P}{\beta^2} - 1 \right)}. \quad (55)$$

It is important to note that C_P , α , and κ_T have a shared denominator: $\mathfrak{F}_{1SQ} + \frac{4\pi^4 Q^4}{5\beta^4 S^4} \mathfrak{F}_{3SQ} + \frac{(2b + \sqrt{\frac{S}{\pi}})\pi^{3/2}}{2\beta^2 S^{3/2}} - \frac{4\pi P}{\beta^2} - 1$. This implies that both α and κ_T may diverge at the critical point, similar to how the specific heat at constant pressure behaves when $\mathfrak{F}_{1SQ} + \frac{4\pi^4 Q^4}{5\beta^4 S^4} \mathfrak{F}_{3SQ} + \frac{(2b + \sqrt{\frac{S}{\pi}})\pi^{3/2}}{2\beta^2 S^{3/2}} - \frac{4\pi P}{\beta^2} - 1 = 0$.

We will now examine the validity of the Ehrenfest equations (Eqs. (49) and (50)) at the critical point. To do this, we will utilize the definition of the volume expansion coefficient α (Eq. (51)), leading to the following relationship

$$V\alpha = \left(\frac{\partial V}{\partial T} \right)_P = \left(\frac{\partial V}{\partial S} \right)_P \left(\frac{\partial S}{\partial T} \right)_P = \left(\frac{\partial V}{\partial T} \right)_P \frac{C_P}{T}, \quad (56)$$

where $\frac{C_P}{T} = \left(\frac{\partial S}{\partial T} \right)_P$. Applying the above equation, we rewrite the R.H.S of Eq. (49) as the following form

$$\frac{\Delta C_P}{VT\Delta\alpha} = \left(\frac{\partial S}{\partial V} \right)_P \Big|_c, \quad (57)$$

where the footnote "c" denotes the values of physical quantities at the critical point. Applying Eqs. (24), and (39), within (57), we find that

$$\frac{\Delta C_P}{VT\Delta\alpha} = \frac{\sqrt{\pi}}{2\sqrt{S}}. \quad (58)$$

Using Eq. (38), the L.H.S of Eq. (49) is given by

$$\left(\frac{\partial P}{\partial T} \right)_S = \frac{\sqrt{\pi}}{2\sqrt{S}}. \quad (59)$$

Equations (58) and (59) demonstrate that the first Ehrenfest equation remains valid at the critical point.

We will verify the validity of the second Ehrenfest equation. To do this, we utilize the thermodynamic identity $\left(\frac{\partial V}{\partial P} \right)_T \left(\frac{\partial P}{\partial T} \right)_V \left(\frac{\partial T}{\partial V} \right)_P = -1$, as reported in Ref. [126]. By applying this identity alongside Eqs. (51)-(55), we can express the R.H.S of Eq. (50) in the following form

$$\frac{\Delta\alpha}{\Delta\kappa_T} = \left(\frac{\partial P}{\partial T} \right)_P \Big|_c = \frac{\sqrt{\pi}}{2\sqrt{S}}. \quad (60)$$

The L.H.S of Eq. (50), is given by

$$\left(\frac{\partial P}{\partial T} \right)_V \Big|_c = \frac{\sqrt{\pi}}{2\sqrt{S}}, \quad (61)$$

where we consider the equation (38) to obtain the above relation. By comparing Eqs. (60) and (61), we find that the second Ehrenfest equation holds at the critical point.

The Prigogine–Defay (PD) ratio is defined as [127, 128]

$$\Pi = \frac{\Delta C_P \Delta\kappa_T}{VT(\Delta\alpha)^2}, \quad (62)$$

by replacing Eqs. (58) and (60) within PD ratio (Eq. (62)), we find that

$$\Pi = 1, \quad (63)$$

The PD ratio quantitatively assesses deviations from the second Ehrenfest equation. For a typical second-order phase transition, this ratio is equal to unity [129]. Based on this analysis, the conclusions drawn from Eq. (63) and the inherent consistency of the Ehrenfest relations lead us to conclude that the transition at the $P - V$ critical point in the extended phase space of the BI-NED AdS black hole surrounded by PFDM is fundamentally a second-order transition.

VI. HEAT ENGINE

Considering BI-NED AdS black hole surrounded by PFDM as a thermodynamic system in the extended phase space, it is natural to assume it as a heat engine [87–105]. A heat engine is a physical system that takes some heat (Q_H) from a warm reservoir converts some of this thermal energy to useful work (W), and transfers the remaining heat energy (Q_C) to the cold reservoir.

The efficiency of heat engine is defined as

$$\eta = \frac{W}{Q_H} = 1 - \frac{Q_C}{Q_H}, \quad (64)$$

where $Q_H = Q_C + W$. Also, the heat engine efficiency depends on the choice of a closed path in the $P - V$ diagram (which is known as a cycle) and the equation of the state of the black hole in question. So, there are different classical cycles, where some of these cycles involve a pair of isotherms at temperatures T_H and T_C (where $T_H > T_C$). For example, in the Carnot cycle (the simplest cycle), there is a pair of isotherms with different temperatures. Using different methods, one can connect these two systems: i) The first method is an isochoric path (like the classical Stirling cycle). ii) The second one is an adiabatic path (like the classical Carnot cycle). Indeed, the form of the path for the definition of the cycle is important. According to this fact, the thermodynamic volume is proportional to entropy (Eq. 39), which leads to the same behavior between adiabatic and isochoric processes. In other words, Carnot and Stirling methods coincide with each other, and calculating efficiency is straightforward in this case [87, 88]. So, we consider the mentioned cycle in Fig. 5.

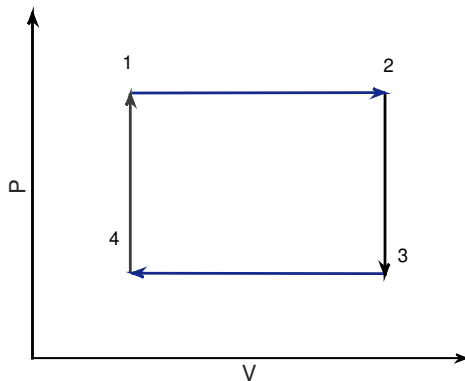


FIG. 5: $P - V$ diagram for Carnot cycle which consists two isobars (paths of $1 \rightarrow 2$ and $3 \rightarrow 4$) and two isochores (paths of $2 \rightarrow 3$ and $4 \rightarrow 1$).

We calculate the work done along the heat cycle as

$$\begin{aligned} W &= PdV = W_{1 \rightarrow 2} + W_{2 \rightarrow 3} + W_{3 \rightarrow 4} + W_{4 \rightarrow 1} = W_{1 \rightarrow 2} + W_{3 \rightarrow 4} \\ &= P_1 (V_2 - V_1) + P_4 (V_4 - V_3), \end{aligned} \quad (65)$$

where $W_{2 \rightarrow 3} = W_{4 \rightarrow 1} = 0$. It means that the work done along paths of $2 \rightarrow 3$ and $4 \rightarrow 1$ are zero because $V_3 - V_2 = 0$, and $V_4 - V_1 = 0$. Using Eq. (39), we can get the work done along the heat cycle as

$$W = \frac{4}{3\sqrt{\pi}} (P_1 - P_4) (S_2^{3/2} - S_1^{3/2}). \quad (66)$$

The upper isobar will give the heat input in the following form

$$Q_H = \int_{T_1}^{T_2} P(P_1, T) dT = \int_{S_1}^{S_2} C_P(P_1, T) \left(\frac{\partial T}{\partial S} \right) dS. \quad (67)$$

where C_P is the heat capacity and is obtained as $C_P(P_1, T) = \frac{2 \left(\tilde{\mathfrak{F}}_{1SQ} + \frac{2\pi^2 Q^2}{\beta^2 S^2} \tilde{\mathfrak{F}}_{2SQ} - \frac{(b + \sqrt{\frac{a}{\pi}}) \pi^{3/2}}{2\beta^2 S^{3/2}} - \frac{4\pi P_1 - 1}{\beta^2} \right) S}{\tilde{\mathfrak{F}}_{1SQ} + \frac{4\pi^4 Q^4}{5\beta^4 S^4} \tilde{\mathfrak{F}}_{3SQ} + \frac{(2b + \sqrt{\frac{a}{\pi}}) \pi^{3/2}}{2\beta^2 S^{3/2}} - \frac{4\pi P_1 - 1}{\beta^2}}$. So, the

heat input is given by

$$\begin{aligned}
Q_H &= \left(\frac{\beta^2}{3} (1 - \mathfrak{F}_{1_{S_2 Q}}) + \frac{4\pi P_1}{3} \right) \left(\frac{S}{\pi} \right)^{3/2} + \frac{b \ln \left(\sqrt{\frac{S}{\pi}} \right) + \sqrt{\frac{S}{\pi}}}{2} \Big|_{S_1}^{S_2} \\
&= \frac{\left(\frac{\beta^2}{3} + \frac{4\pi P_1}{3} \right) (S_2^{3/2} - S_1^{3/2})}{\pi^{3/2}} + \frac{S_2^{1/2} - S_1^{1/2}}{2\pi^{1/2}} + \frac{b}{4} \ln \left(\frac{S_2}{S_1} \right) + \frac{\beta^2}{3\pi^{3/2}} (S_1^{3/2} \mathfrak{F}_{1_{S_1 Q}} - S_2^{3/2} \mathfrak{F}_{1_{S_2 Q}}), \quad (68)
\end{aligned}$$

where $\mathfrak{F}_{1_{S_1 Q}} = \mathfrak{F}_{1_{S_2 Q}}|_{S=S_1}$, and $\mathfrak{F}_{1_{S_2 Q}} = \mathfrak{F}_{1_{S_2 Q}}|_{S=S_2}$.

After some calculations, one can get the heat engine efficiency of BI-NED AdS black holes surrounded by PFDM by inserting Eqs. (66) and (68) into Eq. (64), as

$$\eta = \frac{(P_1 - P_4) (S_2^{3/2} - S_1^{3/2})}{\frac{(\beta^2 + 4\pi P_1) (S_2^{3/2} - S_1^{3/2})}{4\pi} + \frac{3(S_2^{1/2} - S_1^{1/2})}{8} + \frac{3b\pi^{1/2}}{16} \ln \left(\frac{S_2}{S_1} \right) + \frac{\beta^2}{4\pi} (S_1^{3/2} \mathfrak{F}_{1_{S_1 Q}} - S_2^{3/2} \mathfrak{F}_{1_{S_2 Q}})}, \quad (69)$$

where it is dependent on both the parameters of PFDM and BI-NED. According to the equation (69), the PFDM' parameter is in the denominator of η . Therefore, when b is increased, the heat engine efficiency decreases if S_2 remains constant (see the left panel of Fig. 6, (Fig. 6a)). Additionally, the heat engine efficiency is sensitive to changes in the BI-NED parameter due to the complexity of the hypergeometric function located in the denominator of η . To illustrate this, we plot η versus S_2 in the right panel of Fig. 6 (Fig. 6b), considering different values of β while keeping the other parameters fixed. Our analysis reveals that η increases with an increase in β at the same value of S_2 . Given that $S_2 > S_1$, an increase in S_2 results in higher heat engine efficiency for all values of b and β .

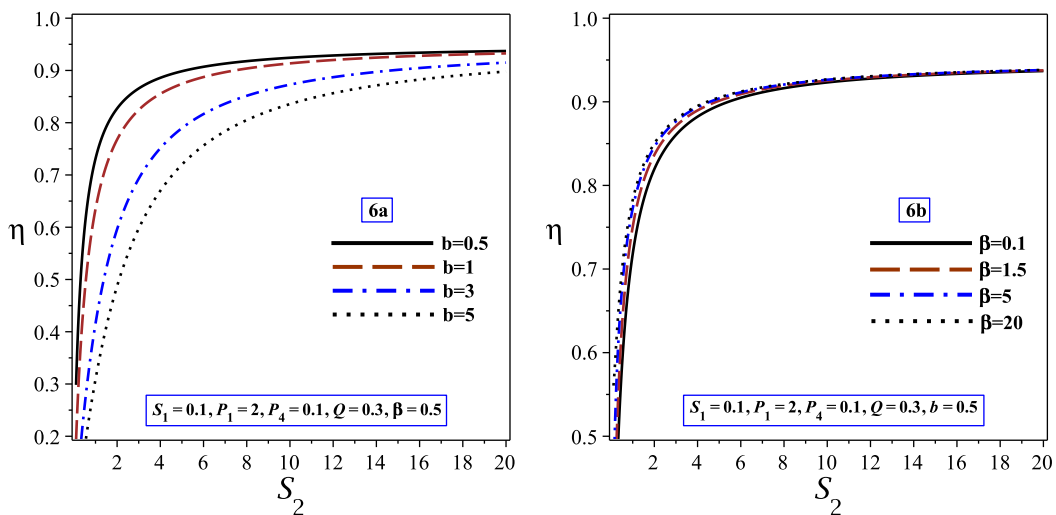


FIG. 6: The heat engine efficiency η versus S_2 for different parameters of b in the left panel and β in the right panel.

The Carnot efficiency is determined as

$$\eta_c = 1 - \frac{T_C}{T_H}, \quad (70)$$

this the maximum efficiency any heat engine can have and any higher efficiency would violate the second law of thermodynamics. To calculate Carnot efficiency, we consider the T_H and T_C in our cycle correspond to T_2 and T_4 , respectively. So, Carnot efficiency is given by

$$\eta_c = 1 - \frac{S_1^{1/2} \left[\mathfrak{F}_{1S_1Q} + \frac{2\pi^2 Q^2 \mathfrak{F}_{2S_1Q}}{\beta^2 S_1^2} - \frac{(b + \sqrt{\frac{S_1}{\pi}}) \pi^{3/2}}{2\beta^2 S_1^{3/2}} - \frac{4\pi P_4}{\beta^2} - 1 \right]}{S_2^{1/2} \left[\mathfrak{F}_{1S_2Q} + \frac{2\pi^2 Q^2 \mathfrak{F}_{2S_2Q}}{\beta^2 S_2^2} - \frac{(b + \sqrt{\frac{S_2}{\pi}}) \pi^{3/2}}{2\beta^2 S_2^{3/2}} - \frac{4\pi P_1}{\beta^2} - 1 \right]}, \quad (71)$$

From the equation (71), it is evident that the behavior of Carnot efficiency is critically dependent on both the parameters of PFDM and BI-NED. To study the effect of PFDM's parameter, we plot Carnot efficiency (η_c) versus S_2 for different values of b in Fig. 7a. Our findings indicate that as b increases, the heat engine efficiency decreases when S_2 remains constant (see Fig. 7a). However, for different values of b , the Carnot efficiency increases and approaches 1 as S_2 becomes very large. In Fig. 7b, we evaluate the effect of the BI-NED parameter on η_c for various values of β . The results show that η_c increases with increasing β when S_2 remains constant. Additionally, η_c approaches 1 as S_2 tends to very large values.

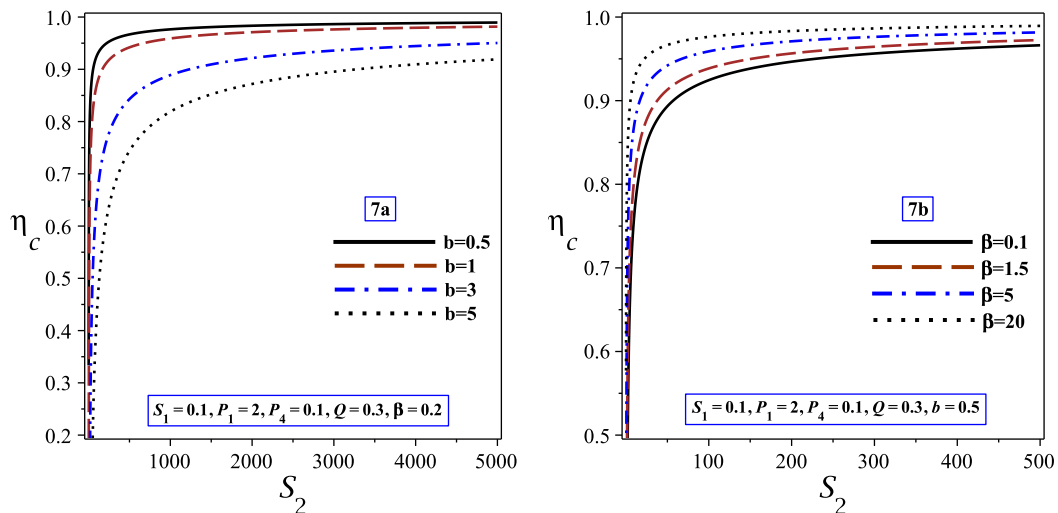


FIG. 7: The Canot efficiency η_c versus S_2 for different parameters of b in the left panel and β in the right panel.

To compare the heat engine efficiency of BI-NED AdS black holes surrounded by PFDM with the Carnot efficiency, we plot the ratio of the efficiencies (η) to the Carnot efficiency (η_c) (i.e., $\frac{\eta}{\eta_c}$) for different values of b and β in Fig. 8a and Fig. 8b, respectively. This ratio cannot exceed 1 ($\frac{\eta}{\eta_c} < 1$), imposing a constraint on the parameters of PFDM. In other words, our findings indicate that we cannot consider very large values for the PFDM parameters because $\frac{\eta}{\eta_c}$ cannot exceed 1. However, the effect of the BI-NED parameter on this ratio shows that there is no constraint for β , as $\frac{\eta}{\eta_c}$ remains less than 1 for all values of the BI-NED parameter.

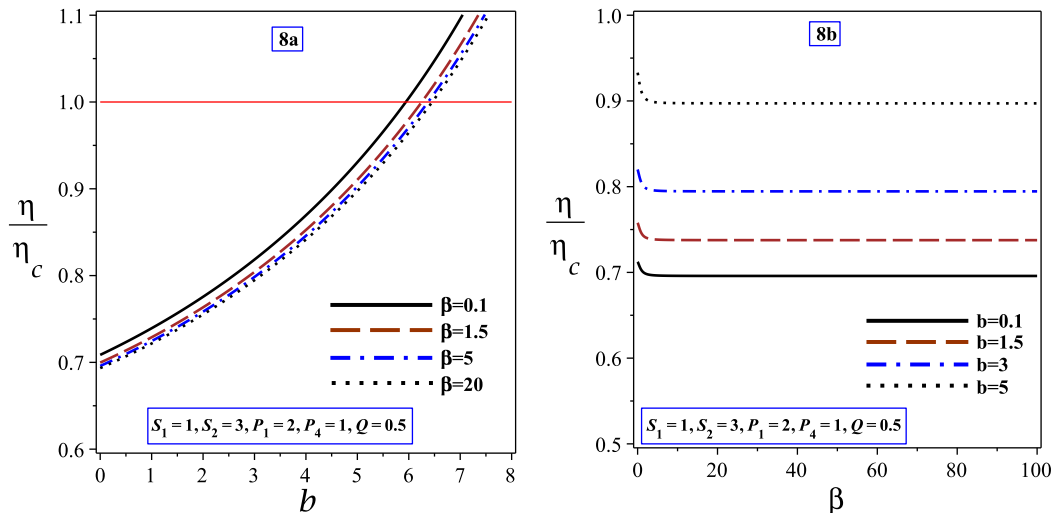


FIG. 8: $\frac{\eta}{\eta_c}$ versus b (in the left panel) and β (in the right panel) are plotted.

VII. TOPOLOGICAL THERMODYNAMIC DEFECTS

In this section, we study the topological classification of the thermodynamic system of our new BI-PFDM-AdS solution. The method employed was developed in the well-known work of Ref. [133]. The approach proposed in [133] introduces a topological classification of black hole solutions based on their thermodynamic structure, reinterpreting equilibrium states as topological defects in parameter space. The construction begins with the definition of a generalised *off-shell* free energy, which depends explicitly on the horizon radius and on external thermodynamic variables, such as the reservoir temperature. Unlike the traditional analysis, the equilibrium condition is not imposed initially; instead, the free energy is regarded as a function defined on a two-dimensional parameter space. The physical black hole solutions correspond to the critical points of this free energy, namely the points where its gradient vanishes.

From this structure, a thermodynamic vector field is defined whose zeros coincide with each equilibrium solution. Each zero is treated as a topological defect, allowing the association of a winding number obtained from the rotation of the vector along a closed contour surrounding the critical point. This number is a topological invariant taking integer values, typically $+1$ or -1 , which are directly related to local thermodynamic stability: positive values correspond to locally stable solutions (positive specific heat), whereas negative values indicate instability.

The central step of the method consists in defining a global topological number W , given by the sum of the winding numbers of all critical points present for a given thermodynamic configuration. This number does not depend on microscopic details or on specific parameter values, but only on the asymptotic behaviour of the temperature in extreme regimes of the horizon radius. In this way, different families of black holes can be classified into universal topological classes characterised by $W = -1$, $W = 0$, or $W = +1$, reflecting respectively the predominance of unstable states, a balance between stable and unstable branches, or the predominance of stable states.

The method therefore establishes a conceptual bridge between black hole thermodynamics and the theory of topological defects, providing a global and robust characterisation of the phase structure that complements the traditional analysis based solely on specific heat or thermodynamic potentials.

Setting $\psi(r_h) = 0$, taking into account $P = -\Lambda/(8\pi)$, and isolating the mass, we obtain

$$M(r_h, q, P) = \frac{1}{6} \left[3r_h + 2r_h^3(4P\pi + \beta^2) - 2r_h^3\beta^2; {}_2F_1[-(3/4), -(1/2), 1/4, -(q^2/(r_h^4\beta^2))] + 3b \ln \left(\frac{r_h}{|b|} \right) \right]. \quad (72)$$

The temperature is then

$$T = \frac{1}{4\pi r_h^2} \left[b + r_h + 2r_h^3 \left(4\pi P + \beta^2 \left(1 - \sqrt{1 + \frac{q^2}{r_h^4 \beta^2}} \right) \right) \right]. \quad (73)$$

We then define the generalised free energy

$$F(r_h, q, P) = M(r_h, q, P) - \frac{\pi r_h^2}{\tau}. \quad (74)$$

When the equations of motion are satisfied, imposing $\frac{\partial F}{\partial r_h} \equiv 0$, we obtain the identity $\tau = T^{-1}$.

Taking a particular example $b = 0.05, \beta = 0.5, q = r_0$, we find the values $r_1 = 0.6234565874733241r_0$, $r_2 = 1.515620115241819r_0$, $r_3 = 3.8684528125703905r_0$, after first solving $\frac{d\tau}{dr_h} = 0$. The corresponding values of τ are respectively $\tau_1 = 28.2502, \tau_2 = 24.2415, \tau_3 = 27.4052$. We represent this example in Fig. 9. One can clearly see the vertical blue dashed lines, where the derivatives of τ vanish. We also observe four phases represented by the red, green, yellow, and dark-blue curves. We now define a two-dimensional vector field

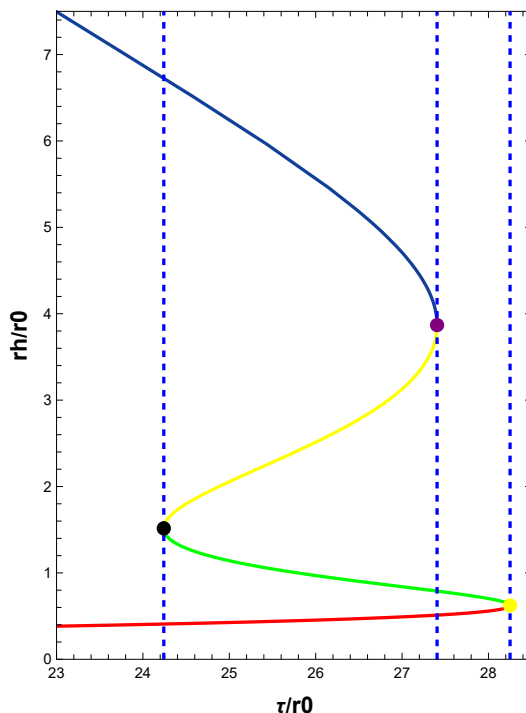


FIG. 9: Representation of $\frac{\tau}{r_0} \times \frac{r_h}{r_0}$.

$$\vec{\Phi} = \{\phi_r, \phi_\theta\}, \quad (75)$$

$$\phi_r = \frac{\partial F}{\partial r_h}, \quad \phi_\theta = -\cot \theta \csc \theta. \quad (76)$$

Normalising, we obtain

$$\vec{N} = \{N_r, N_\theta\}, \quad (77)$$

$$N_r = \frac{\phi_r}{\sqrt{\phi_r^2 + \phi_\theta^2}}, \quad N_\theta = \frac{\phi_\theta}{\sqrt{\phi_r^2 + \phi_\theta^2}}. \quad (78)$$

The zeros of this vector field are the points separating the thermodynamic phases.

We now take the values $r_h = r_0, b = 0.05, \beta = 0.5, q = r_0, P = 0.0022/r_0^2, \tau = 26r_0$ (following the original reference [133]). We can then represent the vector field as a function of $\theta \times \frac{r_h}{r_0}$ using the `VectorPlot` command in the Mathematica software, resulting in Fig. 10. One can clearly see in the figure that at all phase transition points

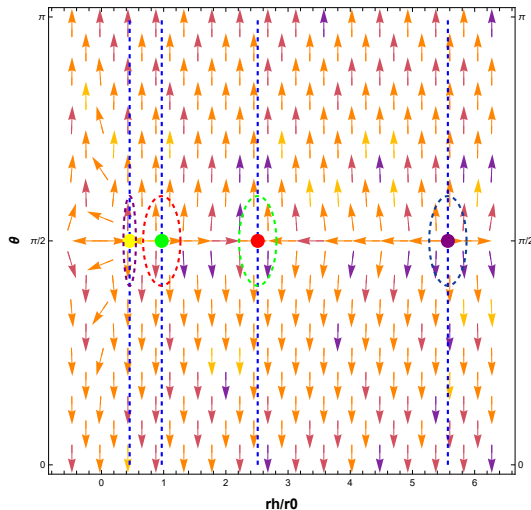


FIG. 10: Representation of the vector field \vec{N} .

the field \vec{N} vanishes and changes orientation. The vertical blue dashed curves represent the values of topological phase transition, namely $r_1 = 0.45348689451390667$, $r_2 = 0.9695037375490816$, $r_3 = 2.512179349141056$, $r_4 = 5.569267583344496$. The yellow, green, red, and purple points represent the zeros of the vector field.

We now integrate a curve around each point in order to calculate the winding numbers for each specific contour. These numbers are topological invariants and are independent of the contour. We use the following parametrisation for each contour

$$r = r_i + k_i \cos(z), \quad (79)$$

$$\theta = \frac{\pi}{2} + p_i \cos(z), \quad (80)$$

with $z \in [0, 2\pi]$ and k_i, p_i positive real numbers, and r_i the values at which the vector field vanishes. Defining

$$F(z) = \eta^{ij} N_i \frac{dN_j}{dz}, \quad i, j = r, \theta, \quad (81)$$

where η^{ij} is the Levi-Civita tensor in this space, we define the winding numbers as

$$w_i = \frac{1}{2\pi} \int_0^{2\pi} F(z) dz. \quad (82)$$

Finally, summing all winding numbers, we obtain the topological invariant number that characterises the thermodynamic system of the black hole

$$W = \sum_i w_i. \quad (83)$$

We now choose the contours such that $k_1 = p_1 = 0.1$ and $k_2, k_3, k_4 = 0.3$. Performing the numerical integration, we obtain the winding numbers

$$w_1 = w_3 = -1, \quad w_2 = w_4 = 1. \quad (84)$$

Therefore, the topological number is

$$W = 0. \quad (85)$$

We conclude that there exist four distinct phases, with two locally stable ones (second and fourth) and two locally unstable ones (first and third). This already occurred in the case of the BI-AdS black hole [132], which characterises the reentrant phase transition. The most important result is that this behaviour classifies the topology of the thermodynamic system of our BIPFDM-AdS solution as being in equilibrium between unstable and stable states, with topological number $W = 0$.

VIII. TIMELIKE GEODESICS

A free test particle moves around a black hole along time-like geodesics. The corresponding geodesic equations can be obtained either via the Hamilton-Jacobi formalism or by employing the Euler-Lagrange equations; here, we follow the latter approach as described in detail by Chandrasekhar [130]. For a general static, spherically symmetric spacetime, the Lagrangian for a point particle reads

$$2\mathcal{L} = g_{\mu\nu}\dot{x}^\mu\dot{x}^\nu = -\psi(r)\dot{t}^2 + \frac{\dot{r}^2}{\psi(r)} + r^2\left(\dot{\theta}^2 + \sin^2\theta\dot{\varphi}^2\right), \quad (86)$$

where the dot denotes differentiation with respect to the affine parameter τ . The generalized momentum is then defined as

$$p_\mu = \frac{\partial\mathcal{L}}{\partial\dot{x}^\mu} = g_{\mu\nu}\dot{x}^\nu. \quad (87)$$

The spacetime admits two Killing vectors, ∂_t and ∂_φ , giving rise to two constants of motion: the energy ε and the orbital angular momentum L , which satisfy

$$p_t = g_{00}\dot{t} = -\varepsilon, \quad (88)$$

$$p_\varphi = g_{\varphi\varphi}\dot{\varphi} = L. \quad (89)$$

These equations yield

$$\dot{t} = \frac{\varepsilon}{\left(1 - \frac{2m_0}{r} - \frac{\Lambda r^2}{3} + \frac{2\beta^2 r^2(1-\mathfrak{F}_1)}{3} + \frac{b}{r} \ln\left(\frac{r}{|b|}\right)\right)}, \quad (90)$$

$$\dot{\varphi} = \frac{L}{r^2 \sin^2\theta}. \quad (91)$$

For timelike geodesics, imposing $g_{\mu\nu}\dot{x}^\mu\dot{x}^\nu = -1$, and restricting motion to the equatorial plane $\theta = \frac{\pi}{2}$ and $\dot{\theta} = 0$, the radial equation takes the form

$$\dot{r}^2 = \varepsilon^2 - \left(1 - \frac{2m_0}{r} - \frac{\Lambda r^2}{3} + \frac{2\beta^2 r^2(1-\mathfrak{F}_1)}{3} + \frac{b}{r} \ln\left(\frac{r}{|b|}\right)\right) \left(1 + \frac{L^2}{r^2}\right). \quad (92)$$

This can be expressed as a one-dimensional motion equation:

$$\dot{r}^2 = \varepsilon^2 - V_{\text{eff}}(r), \quad (93)$$

where the effective potential is

$$V_{\text{eff}}(r) = \left(1 - \frac{2m_0}{r} - \frac{\Lambda r^2}{3} + \frac{2\beta^2 r^2(1-\mathfrak{F}_1)}{3} + \frac{b}{r} \ln\left(\frac{r}{|b|}\right)\right) \left(1 + \frac{L^2}{r^2}\right), \quad (94)$$

The effective potential governs the geodesic structure, with circular orbits corresponding to its local extrema. Figure 11 depicts $V_{\text{eff}}(r)$ for Born-Infeld AdS black holes surrounded by perfect fluid dark matter. For each combination of b and β , the potential exhibits a minimum and a maximum corresponding to stable and unstable circular orbits, respectively. Increasing b enhances the potential barrier, reflecting the stronger gravitational effect of the surrounding dark matter, whereas the BI parameter β shows only a very weak dependence, indicating a negligible contribution from the Born-Infeld electromagnetic field.

We analyze the possible orbits of a massive test particle around Born-Infeld AdS black holes surrounded by perfect fluid dark matter by solving Eq. (92) numerically. In Fig.12, we present the corresponding effective potential. Depending on the initial energy and position of the particle, different types of orbital motion are obtained:

- For $\varepsilon > \varepsilon_{uns}$, the particle falls directly into the singularity from rest at a finite distance. In this case, a plunge orbit occurs in which the particle approaches from infinity, partially orbits the black hole, and ultimately spirals into the center.

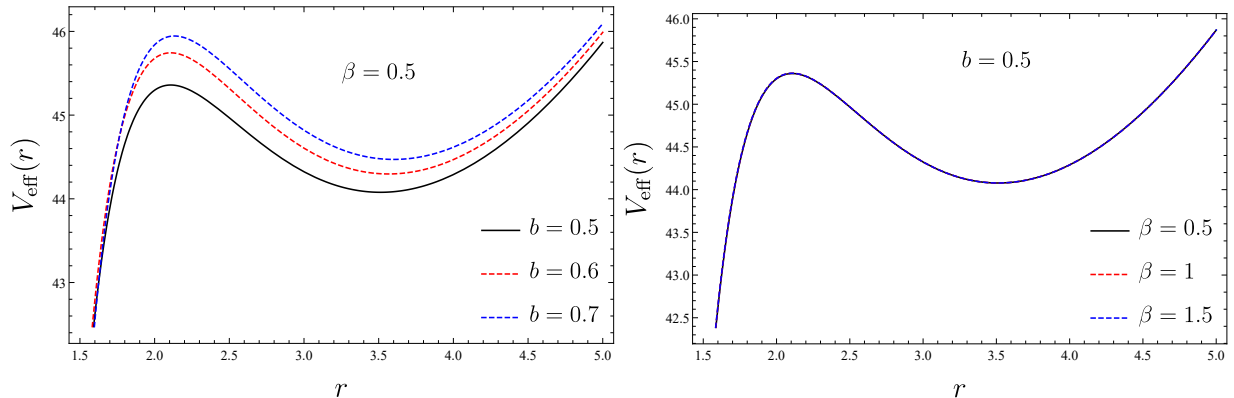


FIG. 11: Effective $V_{\text{eff}}(r)$ potential for timelike geodesics of a massive particle around the BI AdS black hole surrounded by PFDM. Here we take: $m_0 = 1$, $q = 0.5$, $L = 10$ and $\Lambda = -1$

- For $\varepsilon = \varepsilon_{uns}$, the particle occupies an unstable circular orbit; small perturbations in the initial conditions determine whether it falls into the singularity or moves away.
- For $\varepsilon = \varepsilon_1$, the particle exhibits bounded motion between A (perihelion) and B (aphelion), corresponding to a stable oscillatory orbit.
- For $\varepsilon = \varepsilon_{sta}$, the particle remains in a stable circular orbit.

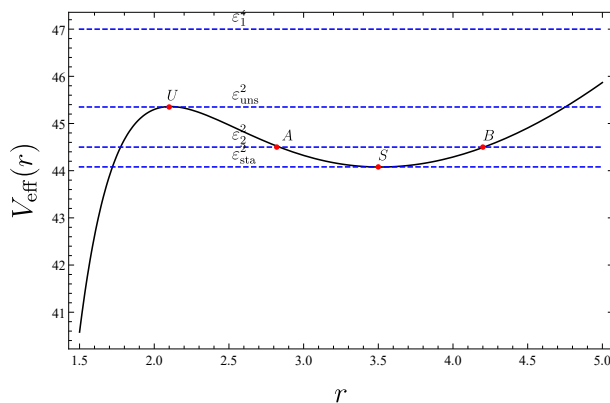


FIG. 12: The relation between the energy levels ε and the effective potential $V_{\text{eff}}(r)$.

In fig.13 we illustrate the unstable circular orbit for different initial angular velocities, with initial conditions $\{0, U, \frac{\pi}{2}, \frac{\pi}{4}\}$. A critical value $\dot{\varphi}(0) \simeq 2.2678$ is identified: for $\dot{\varphi}(0)$ above this threshold, the particle does not cross the horizon, whereas for smaller values it plunges inward.

Fig.14 shows the unstable circular orbit for the initial conditions $\{0, S, \frac{\pi}{2}, \frac{\pi}{4}\}$ for different initial angular velocities. The particle does not cross the horizon. However, small perturbations destabilize the trajectory, leading either to capture by the black hole or to escape.

In Fig.15 we plot the bound orbits for the initial conditions $\{0, A, \frac{\pi}{2}, \frac{\pi}{4}\}$ for different initial angular velocities. In this case, the particle does not cross the horizon but instead moves in a bounded trajectory within the radial range $A \leq r \leq B$, where A represents the perihelion distance and B the aphelion distance. These correspond to planetary-type orbits.

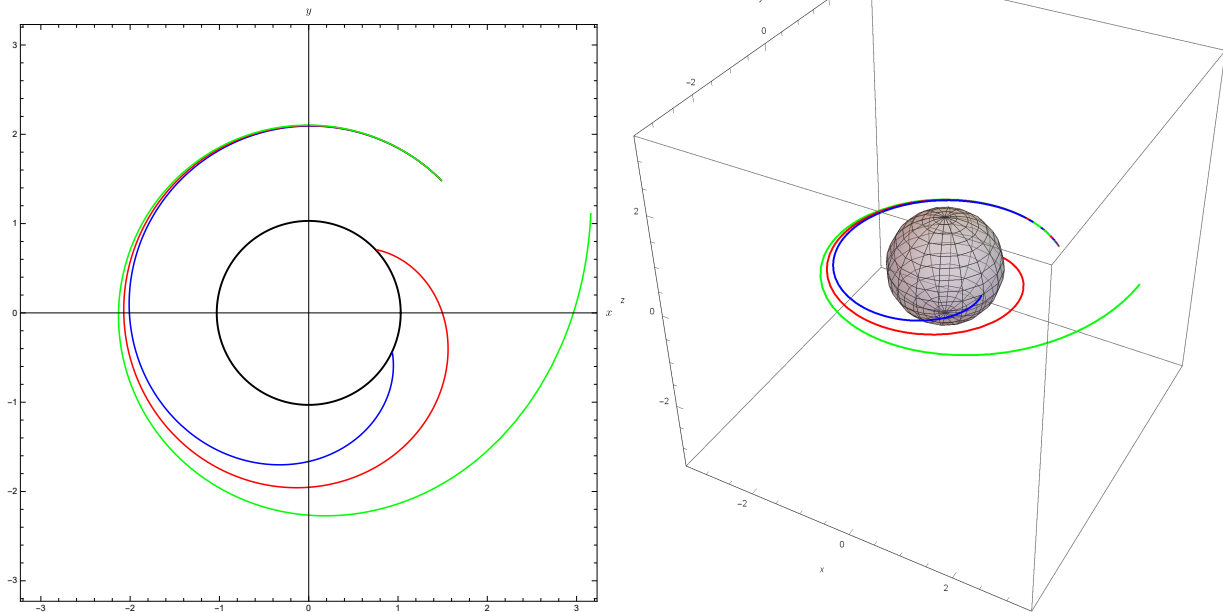


FIG. 13: The unstable circular orbits for different initial velocities. Blue line $\dot{\varphi}(0) = 2.1678$, Red line $\dot{\varphi}(0) = 2.2678$, Green line $\dot{\varphi}(0) = 2.3678$

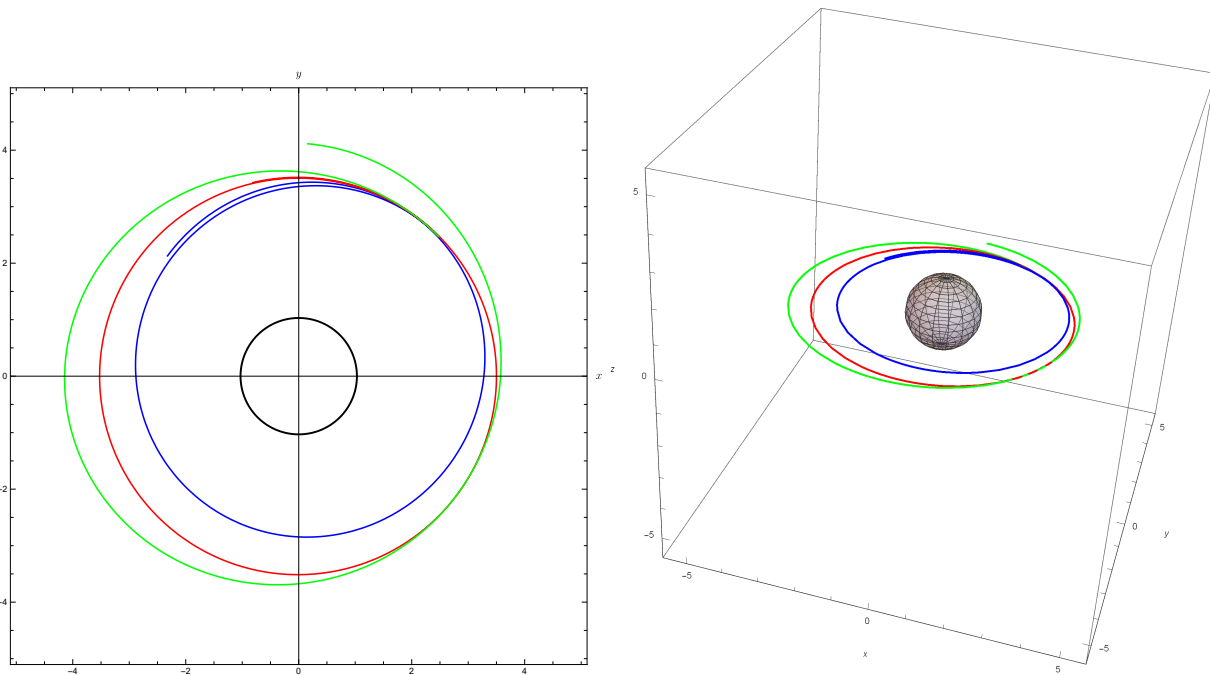


FIG. 14: The stable circular orbits for different initial velocities. Blue line $\varphi(0) = 0.7165$, Red line $\varphi(0) = 0.7165$, Green line $\varphi(0) = 0.9165$

We now consider the circular motion of a massive particle confined to the equatorial plane. For a circular orbit, the radial coordinate remains constant, implying $\dot{r} = 0$ and $\ddot{r} = 0$. Under these conditions, Eq. (93) yields $V_{\text{eff}}(r) = \varepsilon^2$. Furthermore, imposing the extremum condition $\frac{\partial}{\partial r} V_{\text{eff}}(r) = 0$, the specific energy and specific angular momentum of the particle can be expressed as

$$\varepsilon^2 = \frac{2\psi(r)^2}{2\psi(r) - r\psi'(r)}, \quad (95)$$

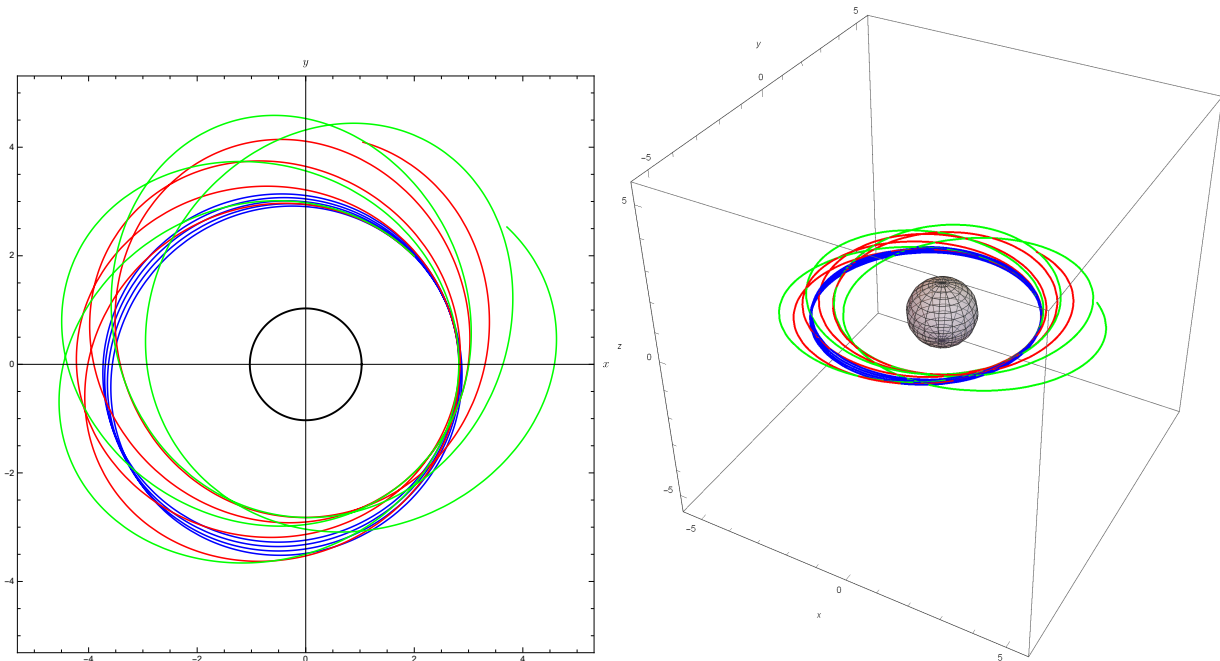


FIG. 15: The bound orbits for different initial velocities. Blue line $\varphi(0) = 1.158$, Red line $\varphi(0) = 1.258$, Green line $\varphi(0) = 1.358$

$$L^2 = \frac{r^3 \psi'(r)}{2\psi(r) - r\psi'(r)}, \quad (96)$$

while the angular velocity of the particle is given by

$$\Omega_\varphi = \frac{d\varphi}{dt} = \sqrt{\frac{\psi'(r)}{2r}}. \quad (97)$$

A circular orbit is stable if the effective potential exhibits a minimum and unstable if it corresponds to a maximum. Tables I summarize the dependence of the stable and unstable circular orbit radii on the PFDM parameter b and BI-NED parameter β , respectively. For fixed β , the stable radius r_{stable} shows a non-monotonic behaviour with increasing b : it first increases, reaches a maximum around $b \sim 1$, and then decreases for larger values of b , indicating the existence of a critical dark matter strength at which the orbital configuration undergoes a qualitative modification. Meanwhile, the unstable circular orbit radius first decreases, reaches a minimum and then increases. In contrast, for fixed b , the variation of the unstable radius and stable radius with respect to the BI parameter β shows very weak dependence. As β increases, the unstable radius decreases slightly, whereas the stable radius remains nearly constant with negligible change. Overall, the PFDM parameter induces global and potentially bifurcation-like modifications in the geodesic structure, whereas the BI-NED parameter has a negligible influence on the stable and unstable orbit radii.

$\beta = 0.5$			$b = 0.5$		
b	r_{uns}	r_{sta}	β	r_{uns}	r_{sta}
0.2	2.54583	3.0049	0.2	2.11421	3.51165
0.4	2.14641	3.43033	0.4	2.10863	3.51198
0.6	2.10759	3.56575	0.6	2.10747	3.51204
0.8	2.17506	3.62133	0.8	2.10706	3.51207
1.0	2.30015	3.62803	1.0	2.10686	3.51208
1.2	2.47019	3.5911	1.2	2.10676	3.51208
1.4	2.69731	3.49522	1.4	2.10669	3.51208

TABLE I: Radii of stable and unstable circular orbits. Parameters $m_0 = 1$, $q = 0.5$, $\Lambda = -1$ and $L = 10$.

The most astrophysically relevant class of trajectories are the innermost stable circular orbits (ISCOs), which determine the inner edge of accretion disks. The ISCO corresponds to the inflection point of the effective potential $V_{\text{eff}}(r)$, and is therefore obtained from the conditions

$$\frac{\partial^2}{\partial r^2} V_{\text{eff}}(r) = \frac{\partial}{\partial r} V_{\text{eff}}(r) = 0, \quad (98)$$

Solving these equations simultaneously leads to the constraint

$$r\psi(r)\psi''(r) + 3\psi(r)\psi'(r) - 2r\psi(r)^2 \Big|_{r=r_{\text{ISCO}}} = 0. \quad (99)$$

Since this equation cannot be solved analytically in closed form, we investigate it numerically. In Fig. 16 (left panel), we present the variation of the ISCO radius as a function of the PFDM parameter b . The curve exhibits a clear non-monotonic behaviour. For small values of b , r_{ISCO} decreases rapidly as b increases, reaching a minimum at a critical value b_{crit} . Beyond this point, r_{ISCO} increases monotonically with further increase in b . This behaviour signals the existence of a critical dark matter strength at which the ISCO radius attains its smallest value. Physically, this indicates that for moderate PFDM intensity, the effective gravitational attraction is enhanced in such a way that stable circular motion can occur closer to the black hole. However, for larger values of b , the dark matter contribution modifies the global structure of the spacetime and shifts the ISCO outward. The resulting U-shaped profile reflects the competing influence of the logarithmic PFDM term in the metric function, which affects both the near-horizon and intermediate radial regions of the effective potential. This non-monotonic behaviour demonstrates the significant impact of PFDM on the strong-field orbital structure. The dependence of the ISCO radius on the BI-NED parameter β is shown in Fig. 16 (right panel). For very small values of β , corresponding to the strongly nonlinear electrodynamic regime, r_{ISCO} decreases smoothly and reaches a minimum at an intermediate value of the parameter.

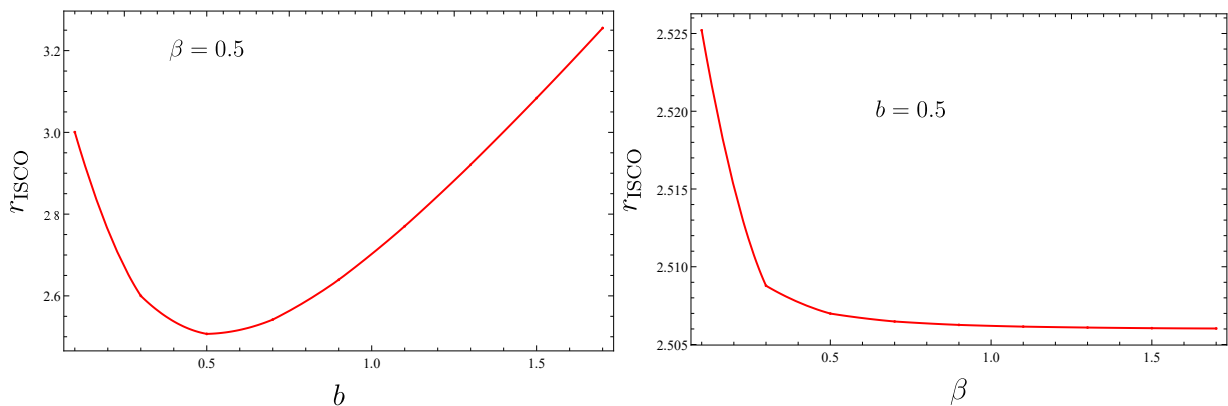


FIG. 16: Variation of the innermost stable circular orbit radius r_{ISCO} as a function of the PFDM parameter b (left) and the BI parameter β (right). Here we take: $m_0 = 1$, $q = 1.5$, $\beta = 0.55$.

A. The effective force

The effective force governing the motion of a test particle plays a crucial role in determining the nature of its trajectory, as it characterizes whether the particle is subject to gravitational attraction or experiences repulsive effects in the vicinity of the black hole. The effective force is derived from Eq. (94) by taking the radial derivative of the effective potential, and is given by

$$F(r) = -\frac{1}{2} \frac{d}{dr} V_{\text{eff}}(r) = \left(\frac{1}{r} - \frac{2m_0}{r^2} + \frac{2\Lambda r}{3} + \frac{3b}{2r^2} \ln\left(\frac{r}{|b|}\right) - \frac{b}{2r^2} + \frac{2q^2 \mathfrak{F}_2}{r^3} \right) \frac{L^2}{r^2} - \frac{m_0}{r^2} + \frac{\Lambda r}{3} - \frac{b}{2r^2} + \frac{b}{2r^2} \ln\left(\frac{r}{|b|}\right) - \frac{2\beta^2 r (1 - \mathfrak{F}_1)}{3} + \frac{2q^2 \mathfrak{F}_2}{r^3}. \quad (100)$$

The effective force $F(r)$ as a function of the radial coordinate r is displayed in Fig.17. In the left panel, increasing the PFDM parameter b leads to a noticeable enhancement of the peak amplitude of the force, indicating a stronger

gravitational influence due to the surrounding dark matter. In contrast, as shown in the right panel, variations of the BI parameter β produce only marginal modifications of the force profile, suggesting that the nonlinear electrodynamic effects remain subdominant in the considered parameter range.

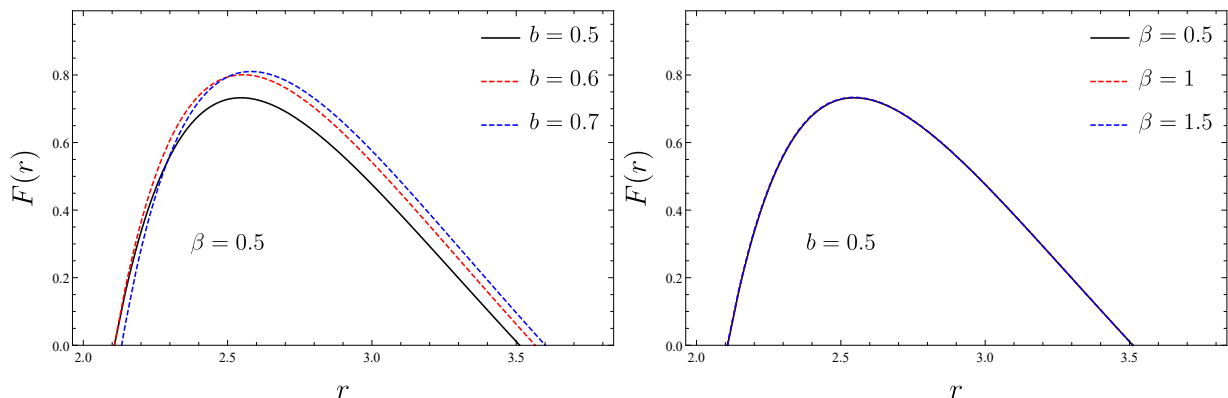


FIG. 17: Radial effective force $F(r)$ acting on a test particle around the BI-NED AdS black hole surrounded by PFDM. Here we take: $m_0 = 1$, $q = 0.5$, $L = 10$ and $\Lambda = -1$

IX. NULL GEODESICS

In general relativity, photon trajectories are described by the null geodesics of the background spacetime. However, in NED, photons do not propagate along the null geodesics of the original metric. Instead, due to self-interaction of the electromagnetic field, they follow null geodesics of an effective geometry determined by the nonlinear structure of the theory. This effective metric depends explicitly on the particular NED model under consideration. Following the formalism of Novello et al. [131], the photon trajectory is obtained by analyzing the propagation of discontinuities in the first derivatives of the electromagnetic field, which propagate along the wave vector k^μ satisfying the null condition

$$\hat{g}^{\mu\nu} k_\mu k_\nu = 0, \quad (101)$$

where the effective metric is given by

$$\hat{g}^{\mu\nu} = (L_{\mathcal{F}} g^{\mu\nu} - 4L_{\mathcal{F}\mathcal{F}} F^{\mu\alpha} F_\alpha^\nu), \quad (102)$$

with $L_{\mathcal{F}\mathcal{F}} = \frac{d^2}{d\mathcal{F}^2} L(\mathcal{F})$. Using the non-vanishing components of the background metric and the electromagnetic field, the effective metric for the BI-NED model takes the form

$$ds^2 = \hat{g}_{00} dt^2 + \hat{g}_{rr} dr^2 + \hat{g}_{\theta\theta} d\theta^2 + \hat{g}_{\varphi\varphi} d\varphi^2, \quad (103)$$

where the inverse components are

$$\hat{g}^{00} = -\frac{L_{\mathcal{F}} + 4L_{\mathcal{F}\mathcal{F}} H(r)^2}{\psi(r)} = \frac{1}{\psi(r)} \left(1 - \frac{q^2}{\beta^2 r^4}\right) \sqrt{1 + \frac{q^2}{\beta^2 r^4}}, \quad (104)$$

$$g^{rr} = \psi(r) \left(L_{\mathcal{F}} g^{rr} + 4L_{\mathcal{F}\mathcal{F}} H(r)^2\right) = -\psi(r) \left(1 - \frac{q^2}{\beta^2 r^4}\right) \sqrt{1 + \frac{q^2}{\beta^2 r^4}}, \quad (105)$$

$$\hat{g}^{\theta\theta} = \frac{L_{\mathcal{F}}}{r^2} = -\frac{1}{r^2} \sqrt{1 + \frac{q^2}{\beta^2 r^4}}, \quad (106)$$

$$\hat{g}^{\varphi\varphi} = -\frac{1}{r^2 \sin^2 \theta} \sqrt{1 + \frac{q^2}{\beta^2 r^4}}. \quad (107)$$

We now investigate photon motion in the background of a BI-NED AdS black hole surrounded by PFDM. The dynamics are governed by the null geodesics of the effective metric, which can be derived from the Lagrangian

$$\mathcal{L} = -\frac{1}{2} \frac{1}{\sqrt{1 + \frac{q^2}{\beta^2 r^4}}} \left[-\frac{\psi(r)}{\left(1 - \frac{q^2}{\beta^2 r^4}\right)} \dot{t}^2 + \frac{1}{\left(1 - \frac{q^2}{\beta^2 r^4}\right)} \dot{r}^2 + r^2 \dot{\theta}^2 + r^2 \sin^2 \theta \dot{\varphi}^2 \right]. \quad (108)$$

which, upon substitution of the effective metric components, yields the modified radial and angular equations of motion. Since the metric components are independent of t and φ , two conserved quantities arise: the energy E and angular momentum L , given by

$$E = \frac{\psi(r)}{\left(1 - \frac{q^2}{\beta^2 r^4}\right) \sqrt{1 + \frac{q^2}{\beta^2 r^4}}} \dot{t}, \quad (109)$$

$$L = \frac{r^2 \sin^2 \theta}{\sqrt{1 + \frac{q^2}{\beta^2 r^4}}} \dot{\varphi}. \quad (110)$$

Imposing the null condition $\hat{g}_{\mu\nu} \dot{x}^\mu \dot{x}^\nu = 0$, and restricting to the equatorial plane, the radial equation of motion can be expressed in the standard form

$$\dot{r}^2 + \mathcal{V}_{eff}(r) = 0, \quad (111)$$

where the effective potential is

$$\mathcal{V}_{eff}(r) = \left(1 - \frac{q^4}{\beta^4 r^8}\right) \left[\psi(r) \frac{L^2}{r^2} - \left(1 - \frac{q^2}{\beta^2 r^4}\right) E^2 \right]. \quad (112)$$

This expression explicitly shows how nonlinear electrodynamics modifies photon motion through multiplicative corrections depending on β , thereby altering the structure of null trajectories relative to the Maxwellian case.

In order to find the unstable circular orbits we impose the conditions

$$\mathcal{V}_{eff}(r)|_{r=r_{ph}} = 0; \quad \frac{\partial}{\partial r} \mathcal{V}_{eff}(r) \Big|_{r=r_{ph}} = 0, \quad (113)$$

and check whether $\mathcal{V}_{eff}(r)$ is a maxima at $r = r_{ph}$, that is

$$\frac{\partial^2}{\partial r^2} \mathcal{V}_{eff}(r) \Big|_{r=r_{ph}} < 0, \quad (114)$$

where r_p is the radius of the photon sphere. Using Eq. (112), the first condition leads to the critical impact parameter

$$\xi_{ph} = \frac{L}{E} = r_{ph} \sqrt{\frac{1 - \frac{q^2}{\beta^2 r_{ph}^4}}{\psi(r_{ph})}}. \quad (115)$$

An ingoing photon from infinity with $\xi < \xi_{ph}$ falls into the black hole, while photons with $\xi > \xi_{ph}$ are scattered and can reach an observer at infinity. The second condition leads to

$$\left(1 - \frac{q^2}{\beta^2 r^4}\right) \frac{d}{dr} \ln \left(\frac{\psi(r)}{r^2}\right) - \frac{4q^2}{\beta^2 r^5} \Big|_{r=r_{ph}} = 0. \quad (116)$$

In general Eq.(116) cannot be solved analytically, so we proceed numerically. Figure 18 shows the equatorial photon sphere radius for a BI AdS black hole surrounded by PFDM. For fixed β and varying the PFDM parameter b , the photon sphere radius exhibits a non-monotonic dependence on the PFDM parameter b : for small b , increasing b reduces r_{ph} indicating enhanced gravitational attraction near the black hole. Beyond a critical value b_c , however, r_{ph} increases, reflecting the modification of spacetime geometry by dark matter that shifts the unstable null orbit outward. For fixed $b = 2$ varying BI-NED parameter β , results in a photon sphere radius that increases monotonically with β and approaches a constant for large β indicating that NED effects weaken as β grows. In the large- β limit, the solution reduces to the Reissner-Nordström geometry, leading to saturation of the photon sphere radius. The initial growth of r_{ph} demonstrates that strong NED effects compress the photon orbit inward, while the Maxwell limit restores standard charged black hole behavior.

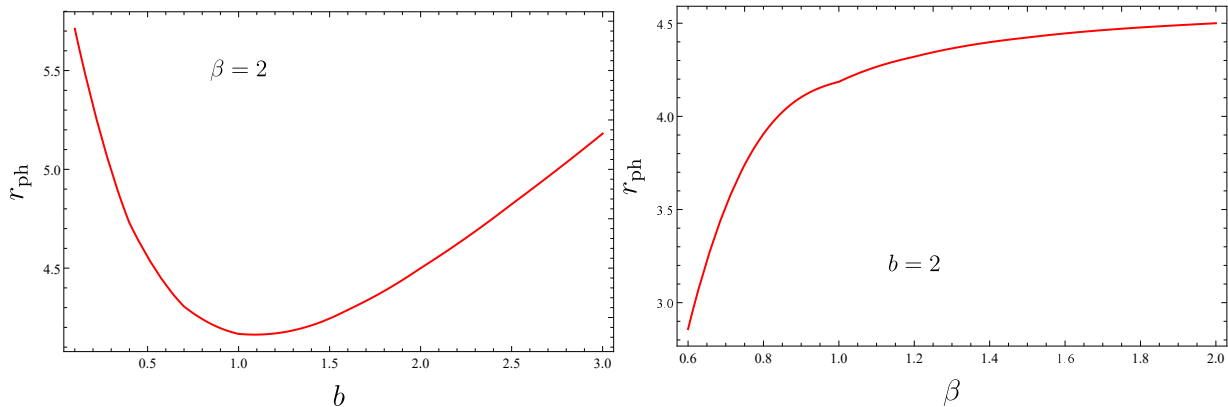


FIG. 18: Radius of the photon sphere r_{ph} as a function of the PFDM parameter b (left) and the BI parameter β (right). Here we take: $m_0 = 2.5$, $q = 1.8$ and $\Lambda = -1$.

Figure 19 shows the critical impact parameter as a function of the radial coordinate. For fixed β , the critical impact parameter exhibits a non-monotonic dependence on b , initially decreasing and then increasing beyond a critical value b_c , reflecting the competing gravitational effects of PFDM. For fixed b the impact parameter increases monotonically with β and saturates at large β , signaling the recovery of the Maxwell limit as nonlinear electrodynamics effects vanish.

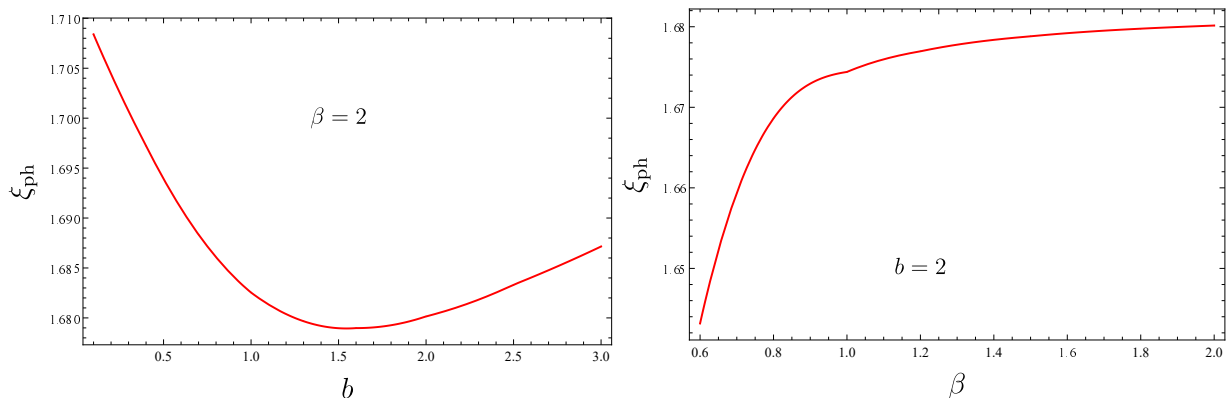


FIG. 19: Critical impact parameter ξ_{ph} as a function of the PFDM parameter b (left) and the BI parameter β (right). Here we take: $m_0 = 2.5$, $q = 1.8$ and $\Lambda = -1$.

For black hole spacetimes possessing a cosmological horizon, such as the Kottler solution, the angular size of the black hole shadow depends explicitly on the radial position of the observer and on the observer's state of motion. For a static observer located at a radial coordinate r_o , the angular radius of the shadow, α_{sh} , is given by

$$\sin \alpha_{\text{sh}} = \sqrt{\frac{g_{\varphi\varphi}(r_{\text{ph}})g_{rr}(r_o)}{g_{rr}(r_{\text{ph}})g_{\varphi\varphi}(r_o)}} = \frac{r_{\text{ph}}}{r_o} \sqrt{\frac{1 - \frac{q^2}{\beta^2 r_{\text{ph}}^4} \psi(r_o)}{1 - \frac{q^2}{\beta^2 r_o^4} \psi(r_{\text{ph}})}}, \quad (117)$$

which can equivalently be written as

$$\sin \alpha_{\text{sh}} = \frac{\xi_{\text{ph}}}{r_o} \sqrt{\frac{\psi(r_o)}{1 - \frac{q^2}{\beta^2 r_o^4}}}. \quad (118)$$

It is important to emphasize that this relation is originally derived in asymptotically flat spacetimes, where null geodesics either escape to infinity or are captured by the black hole. In asymptotically AdS spacetimes, however, the conformal boundary reflects null signals, thereby modifying the global causal structure. Nevertheless, for an observer located at a finite radial distance r_o , the shadow is still predominantly determined by the photon sphere, since the critical impact parameter ξ_{ph} governs photon capture. In this regime, the influence of the AdS boundary on the angular size of the shadow is negligible, and the above expression provides a reliable approximation. Noticeable deviations would arise only for observers situated at very large r_o , where multiple reflections from the AdS boundary may contribute to the observed image.

In the limiting case $r_o = r_{\text{ph}}$, i.e. when the observer is located at the photon sphere, the angular radius satisfies $\alpha_{\text{sh}} = \pi/2$, meaning that the shadow occupies exactly one half of the observer's sky. The behaviour of the static angular radius α_{sh} as a function of r_o is displayed in Fig. 20. In all cases, the shadow angle increases rapidly with increasing r_o , reaches a maximum at an intermediate distance, and subsequently approaches a constant value for large r_o . This behaviour indicates that for observers close to the black hole the apparent shadow size is strongly affected by local spacetime curvature, whereas for distant observers the angular radius converges to an asymptotic value determined primarily by the photon sphere structure.

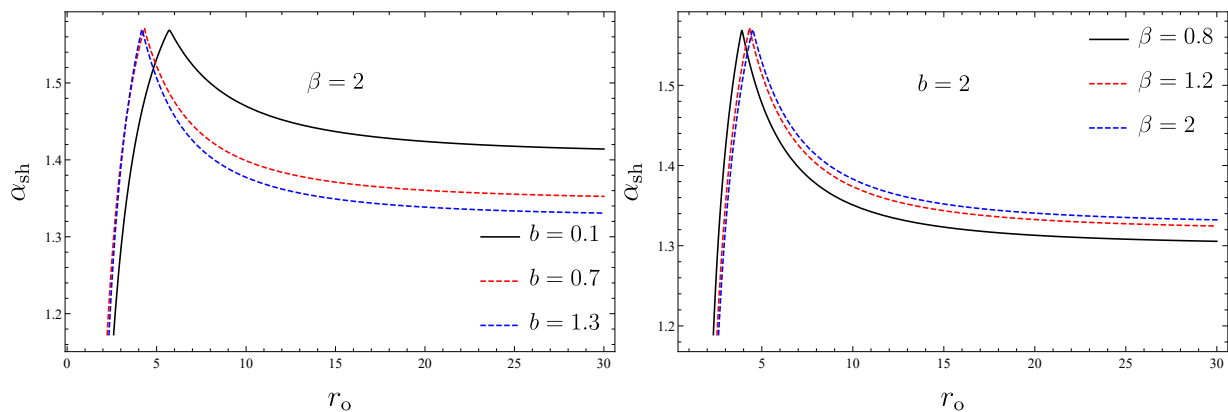


FIG. 20: Angular radius of the black hole shadow α_{sh} versus the PFDM parameter b (left) and the BI parameter β (right). Here we take: $m_0 = 2.5$, $q = 1.8$ and $\Lambda = -1$.

On the other hand, for a static observer located at a radial coordinate r_o , the radius of the black hole shadow is expressed as

$$R_{\text{sh}} = \xi_{\text{ph}} \sqrt{\frac{1 - \frac{2m_0}{r_o} - \frac{\Lambda r_o^2}{3} + \frac{2\beta^2 r_o^2 (1 - \mathfrak{F}_1)}{3} + \frac{b}{r_o} \ln\left(\frac{r_o}{|b|}\right)}{1 - \frac{q^2}{\beta^2 r_o^4}}}. \quad (119)$$

This relation shows that the shadow radius depends explicitly on the observer's position as well as the parameters of the spacetime, including the cosmological constant, the BI-NED parameter, the electric charge, and the PFDM parameter. In the asymptotic limit $r_o \rightarrow \infty$, the shadow radius R_{sh} does not reduce to the critical impact parameter ξ_{ph} , indicating that the presence of the cosmological constant and NED modifies the asymptotic behavior of the shadow compared to the standard asymptotically flat case.

X. DISCUSSION AND CONCLUSION

In this study, we examined Einstein's theory of gravity in the context of a negative cosmological constant and Born-Infeld Nonlinear Electrodynamics (BI-NED), all within a framework that includes a Perfect Fluid Dark Matter

(PFDM) component. By applying this gravitational framework to a static, spherically symmetric scenario in four-dimensional spacetime, we derived exact solutions. These solutions exhibited a singularity at $r = 0$, which was encompassed by at least one event horizon. As a result, we interpreted these solutions as BI-NED AdS black holes surrounded by PFDM.

We analyzed the influence of the PFDM parameter (b) and the BI-NED parameter (β) on the roots of AdS black hole configurations. The results revealed that the horizon structure of these black holes was highly sensitive to variations in b and β . For small b , two horizons appeared, while small β yielded only a single event horizon (similar to Schwarzschild-like black hole). At intermediate values of both parameters, three distinct horizons were observed, representing multi-horizon black holes. When b became large, the geometry approached the Schwarzschild-like limit with one event horizon, whereas large β generated two horizons, resembling the Reissnerâ€“Nordström case. Furthermore, increasing b led to an expansion of the event horizon, while increasing β resulted in its reduction. These findings underscored the coupled role of dark matter effects and nonlinear electrodynamics in shaping the geometric properties of AdS black holes.

By considering BI-NED AdS black holes surrounded by PFDM, we calculated their conserved and thermodynamical quantities—such as Hawking temperature, entropy, charge, electric potential, and total mass. We then examined how the parameters of PFDM and BI-NED affected these quantities and showed that they satisfied the first law of thermodynamics. The effects of b and β on the total mass was very interesting. Indeed, we found that the asymptotic behavior of total mass M remained similar for various values of b , q , and β , as it depended only on the cosmological constant. For the negative values of Λ , the total mass increased with the size of the black hole. In the high-energy limit the behavior of M varied with b : small b yielded a finite positive mass, medium b made M approach zero, and large b produced black holes with $M = 0$ at finite radii shifting outward with increasing b . This demonstrated that the mass of small black holes was highly sensitive to PFDM, differing from Schwarzschild and Reissnerâ€“Nordström cases. Conversely, the BI-NED parameter affected M oppositely—smaller β removed mass divergence and led to finite values, while very large β caused divergent behavior like Reissnerâ€“Nordström black holes. Overall, the divergence of total mass at $r_+ = 0$ disappeared when β decreased or b increased, indicating that PFDM and BI-NED exerted opposite influences on the mass evolution of AdS black holes.

The local thermodynamic stability of BI-NED AdS black holes surrounded by PFDM was analyzed through the simultaneous study of heat capacity and temperature. The results showed that for $b < b_{critical}$, two roots and one divergence point appeared in the heat capacity, where the divergence point was located between the two roots. In this regime, large black holes ($r_+ > r_{0_2}$) satisfied the local stability condition since both heat capacity and temperature were positive. When $b > b_{critical}$, only one divergence point was found, shifting toward larger horizon radii as b increased, and the stability region reduced accordingly. Similarly, for the BI-NED parameter, a critical value existed where two roots and a divergence point occurred when $\beta > \beta_{critical}$, indicating stability for $r_+ > r_{0_2}$. For $\beta < \beta_{critical}$, one divergence point was observed, with C and T positive beyond that point. Overall, the study demonstrated that large BI-NED AdS black holes maintained local thermodynamic stability, while the stability region varied with both PFDM and BI-NED parameters.

We studied the global thermodynamic stability of these black holes through the Helmholtz free energy analysis. For $b < b_{critical}$, two roots of F appeared, where the free energy was negative before the first and after the second root, implying that both small and large black holes satisfied the global stability condition. When $b > b_{critical}$, the free energy remained negative at all radii, meaning the black holes were globally stable. For very large $b \ll b_{critical}$, only large black holes met the global stability requirement. Regarding the BI-NED parameter, increasing β reduced the global stability region, and between two roots, F became positive, indicating instability for medium-sized black holes. As $\beta \rightarrow \infty$, there was a single root where F turned negative beyond it, showing that large BI-NED AdS black holes exhibited global thermodynamic stability for sufficiently large β .

We compared the heat capacity and the Helmholtz free energy together, and we found that the large BI-NED AdS black holes surrounded by PFDM could satisfy the local and global stability conditions simultaneously.

We extended our study to including the cosmological constant as a thermodynamics pressure. In this space (extended phase space), the conserved and thermodynamic quantities were calculated and were found to satisfy the first law of thermodynamics. The specific heat at constant pressure (C_P), the volume expansion coefficient (α), and the isothermal compressibility coefficient (κ_T) were then examined. The results showed that all three quantities shared a common factor in their denominators and diverged at the critical point. The Ehrenfest equations were analytically verified, and both relations were confirmed to be satisfied. Furthermore, the Prigogineâ€“Defay ratio was computed and was found to be exactly equal to one, indicating that the phase transition at the critical point was a second-order transition.

In the extended phase space, the BI-NED AdS black hole surrounded by PFDM was treated as a thermodynamic heat engine. The effects of the PFDM and BI-NED parameters on the heat engine efficiency were examined, and it was found that increasing b led to a decrease in efficiency when S_2 remained constant. The efficiency was shown to depend sensitively on the BI-NED parameter β because of the hypergeometric function in the denominator of η . The

analysis revealed that η increased with increasing β for a fixed S_2 . Since $S_2 > S_1$, an increase in S_2 resulted in higher heat engine efficiency for all values of b and β .

The effects of PFDM and BI-NED parameters on the Carnot efficiency were also studied. The results indicated that as b increased, the heat engine efficiency decreased at constant S_2 , while the Carnot efficiency increased and approached unity as S_2 became very large. Furthermore, η_c increased with increasing β for fixed S_2 and also approached unity for large S_2 .

To compare the efficiencies, the ratio $\frac{\eta}{\eta_c}$ was plotted for different values of b and β . This ratio was found to remain below one, implying a constraint on PFDM parameters: very large values of b were not physically acceptable since $\frac{\eta}{\eta_c} < 1$. However, the BI-NED parameter β imposed no such restriction, as the ratio stayed less than one for all its values.

We have also performed the topological analysis and classification of our new solution, resulting in an equilibrium between stable and unstable states, with four distinct phases, two of them locally stable and two of them locally unstable.

We further explored the motion of massive and massless particles. For timelike geodesics, the effective potential approach shows that the PFDM parameter b significantly modifies the global orbital structure, leading to non-trivial behavior of the stable and unstable circular orbits, including a non-monotonic dependence of the ISCO radius on b . In contrast, the BI-NED parameter β induces a smooth deformation of the strong-field region and governs the transition toward the Maxwell limit. For null geodesics, photon propagation in the effective geometry demonstrates that both PFDM and nonlinear electrodynamics corrections alter the photon sphere radius and consequently the shadow characteristics. The PFDM background mainly affects the large-scale structure of the effective potential, whereas the BI-NED parameter controls near-horizon deviations from linear electrodynamics. These results indicate that the combined effects of dark matter and nonlinear electrodynamics leave distinct imprints on particle dynamics and optical observables, which may provide potential signatures in strong gravitational lensing and black hole shadow measurements.

Acknowledgments

B. Eslam Panah thanks University of Mazandaran. MER thanks Conselho Nacional de Desenvolvimento Científico e Tecnológico – CNPq, Brazil, for partial financial support.

-
- [1] V. A. De Lorenci, and M. A. Souza, Phys. Lett. B **512**, 417 (2001).
 - [2] V. A. De Lorenci, and R. Klippert, Phys. Rev. D **65**, 064027 (2002).
 - [3] M. Novello, and E. Bittencourt, Phys. Rev. D **86**, 124024 (2012).
 - [4] W. Heisenberg, and H. Euler, Z. Phys. **98**, 714 (1936). *Translation by: W. Korolevski and H. Kleinert, Consequences of Dirac's Theory of the Positron*, [arXiv: physics/0605038].
 - [5] H. Yajima, and T. Tamaki, Phys. Rev. D **63**, 064007 (2001).
 - [6] J. Schwinger, Phys. Rev. **82**, 664 (1951).
 - [7] D. H. Delphenich, [arXiv: hep-th/0309108].
 - [8] E. Ayon-Beato, and A. Garcia, Phys. Lett. B **464**, 25 (1999).
 - [9] V. A. De Lorenci, R. Klippert, M. Novello and J. M. Salim, Phys. Rev. D **65**, 063501 (2002).
 - [10] I. Dymnikova, Class. Quantum Gravit. **21**, 4417 (2004).
 - [11] C. Corda, and H. J. Mosquera Cuesta, Astropart. Phys. **34**, 587 (2011).
 - [12] H. H. Soleng, Phys. Rev. D **52**, 6178 (1995).
 - [13] H. P. Oliveira, Class. Quantum Gravit. **11**, 1469 (1994).
 - [14] D. Palatnik, Phys. Lett. B **432**, 287 (1998).
 - [15] E. Ayon-Beato, and A. Garcia, Phys. Rev. Lett. **80**, 5056 (1998).
 - [16] H. J. Mosquera Cuesta, and J. M. Salim, MNRAS **354**, L55 (2004).
 - [17] H. J. Mosquera Cuesta, and J. M. Salim, ApJ **608**, 925 (2004).
 - [18] Z. Bialynicka-Birula, and I. Bialynicka-Birula, Phys. Rev. D **2**, 2341 (1970).
 - [19] S. H. Hendi, B. Eslam Panah, and S. Panahiyan, Phys. Rev. D **91**, 084031 (2015).
 - [20] S. H. Hendi, B. Eslam Panah, M. Momennia, and S. Panahiyan, Eur. Phys. J. C **75**, 457 (2015).
 - [21] M. Born, and L. Infeld, Proc. Roy. Soc. Lond. A **143**, 410 (1934).
 - [22] M. Born, and L. Infeld, Proc. Roy. Soc. Lond. A **144**, 425 (1934).
 - [23] B. Hoffmann, Phys. Rev. **47**, 877 (1935).
 - [24] M. H. Dehghani, and S. H. Hendi, Phys. Rev. D **73**, 084021 (2006).
 - [25] R. G. Cai, and Y. W. Sun, JHEP **09**, 115 (2008).

- [26] S. H. Mazharimousavi, M. Halilsoy, and Z. Amirabi, *Phys. Rev. D* **78**, 064050 (2008).
- [27] S. H. Hendi, *J. Math. Phys.* **49**, 082501 (2008).
- [28] M. H. Dehghani, and H. Rastegar Sedehi, *Phys. Rev. D* **74**, 124018 (2006).
- [29] H. Q. Lu, et al., *Int. J. Theor. Phys.* **42**, 837 (2003).
- [30] M. H. Dehghani, and S. H. Hendi, *Gen. Relativ. Gravit.* **41**, 1853 (2009).
- [31] E. F. Eiroa, and G. F. Aguirre, *Eur. Phys. J. C* **72**, 2240 (2012).
- [32] S. H. Hendi, *Adv. High Energy Phys.* **2014**, 697863 (2014).
- [33] J. Jing, L. Wang, Q. Pan, and S. Chen, *Phys. Rev. D* **83**, 066010 (2011).
- [34] S. Gangopadhyay, and D. Roychowdhury, *JHEP* **05**, 156 (2012).
- [35] W. Yao, and J. Jing, *JHEP* **05**, 058 (2014).
- [36] E. Fradkin, and A. Tseytlin, *Phys. Lett. B* **163**, 123 (1985).
- [37] R. Matsuiev, M. Rahmanov, and A. Tseytlin, *Phys. Lett. B* **193**, 205 (1987).
- [38] E. Bergshoeff, E. Sezgin, C. Pope, and P. Townsend, *Phys. Lett. B* **188**, 70 (1987).
- [39] C. Callan, C. Lovelace, C. Nappi, and S. Yost, *Nucl. Phys. B* **308**, 221 (1988).
- [40] O. Andreev, and A. Tseytlin, *Nucl. Phys. B* **311**, 221 (1988).
- [41] R. Leigh, *Mod. Phys. Lett. A* **04**, 2767 (1989).
- [42] V. V. Kiselev, *Class. Quantum Gravit.* **20**, 1187 (2003).
- [43] C. -K. Qiao, and M. Zhou, *JCAP* **12**, 005 (2023).
- [44] J. Rayimbaev, S. Shaymatov, and M. Jamil, *Eur. Phys. J. C* **81**, 699 (2021).
- [45] B. Hamil, and B. C. Lutfuoglu, *Ann. Phys.* **472**, 169861 (2025).
- [46] Z. Hu, X. Hou, J. Wang, and Y. Liao, *Adv. High Energy Phys.* **2019**, 2434390 (2019).
- [47] X. Hou, Z. Xu, and J. Wang, *JCAP* **12**, 040 (2018).
- [48] M. Rizwan, M. Jamil, and K. Jusufi, *Phys. Rev. D* **99**, 024050 (2019).
- [49] H. X. Zhang, et al., *Chin. Phys. C* **45**, 055103 (2021).
- [50] S. J. Ma, R. -B. Wang, J. -B. Deng, and X. -R. Hu, *Eur. Phys. J. C* **84**, 595 (2024).
- [51] M. R. Shahzad, et al., *Eur. Phys. J. C* **85**, 164 (2025).
- [52] S. Shaymatov, B. Ahmedov, and M. Jamil, *Eur. Phys. J. C* **81**, 588 (2021).
- [53] L. Li, Z. Y. Fu, and H. L. Li, *Gen. Relativ. Grav.* **54**, 43 (2022).
- [54] A. Das, A. Saha, and S. Gangopadhyay, *Class. Quantum Gravit.* **38**, 065015 (2021).
- [55] G. Mustafa, et al., *Phys. Dark Universe.* **46**, 101644 (2024).
- [56] J. Zhang, X. Chen, and J. Tao, *Phys. Dark Universe.* **46**, 101594 (2024).
- [57] A. Ashraf, et al., *Nucl. Phys. B* **1014**, 116873 (2025).
- [58] F. Atamurotov, A. Abdujabbarov, and W. B. Han, *Phys. Rev. D* **104**, 084015 (2021).
- [59] F. Atamurotov, U. Papnoi, and K. Jusufi, *Class. Quantum Gravit.* **39**, 025014 (2022).
- [60] F. Atamurotov, F. Sarikulov, S. G. Gosh, and G. Mustafa, *Phys. Dark Universe.* **46**, 101625 (2024).
- [61] M. Heydari-Fard, S. G. Honarvar, and M. Heydari-Fard, *MNRAS* **521**, 708 (2023).
- [62] G. D. A. Yildiz, et al., *Phys. Dark Universe.* **46**, 101583 (2024).
- [63] G. Rakhimova, et al., *Nucl. Phys. B* **996**, 116363 (2023).
- [64] M. Rizwan, and K. Jusufi, *Eur. Phys. J. C* **83**, 944 (2023).
- [65] A. Das, A. Roy Chowdhury, and S. Gangopadhyay, *Class. Quantum Gravit.* **41**, 015018 (2023).
- [66] H. Chen, et al., *Chin. Phys. C* **48**, 085105 (2024).
- [67] Q. Ama-Tul-Mughani, S. Mumtaz, W. Salam, and A. Ikram, *Int. J. Mod. Phys. D* **31**, 2250046 (2022).
- [68] F. Javed, et al., *Phys. Dark Universe.* **46**, 101656 (2024).
- [69] G. Fatima, et al., *Eur. Phys. J. C* **85**, 208 (2025).
- [70] Y. Feng, et al., *J. High Energy Astrop.* **43**, 158 (2024).
- [71] Y. Y. Sekhmani, et al., *Eur. Phys. J. C* **85**, 229 (2025).
- [72] S. Shaymatov, D. Malafarina, and B. Ahmedov, *Phys. Dark Universe.* **34**, 100891 (2021).
- [73] A. Kumar, et al., *Phys. Dark Universe.* **40**, 101220 (2023).
- [74] A. Sood, Md S. Ali, J. K. Singh, and S. G. Ghosh, *Chin. Phys. C* **48**, 065109 (2024).
- [75] B. Hamil, and B. C. Lutfuoglu, *Chin. Phys. C* **49**, 025107 (2025).
- [76] R. Banerjee, S. K. Modak, and D. Roychowdhury, *JHEP* **10**, 125 (2012).
- [77] R. Banerjee, S. K. Modak, and S. Samanta, *Phys. Rev. D* **84**, 064024 (2011).
- [78] R. Banerjee, S. Ghosh, D. Roychowdhury, *Phys. Lett. B* **696**, 156 (2011).
- [79] D. Kastor, S. Ray, and J. Traschen, *Class. Quantum Grav.* **26**, 195011 (2009).
- [80] B. P. Dolan, *Class. Quantum Grav.* **28**, 125020 (2011).
- [81] B. P. Dolan, *Class. Quantum Grav.* **28**, 235017 (2011).
- [82] D. Kubiznak, and R. B. Mann, *JHEP* **07**, 033 (2012).
- [83] S. Gunasekaran, R. B. Mann and D. Kubiznak, *JHEP* **11**, 110 (2012).
- [84] N. Altamirano, D. Kubiznak and R. B. Mann, *Phys. Rev. D* **88**, 101502 (2013).
- [85] N. Altamirano, D. Kubiznak, R. B. Mann and Z. Sherkatghanad, *Class. Quant. Grav.* **31**, 042001 (2014).
- [86] S. -W. Wei and Y. -X. Liu, *Phys. Rev. D* **90**, 044057 (2014).
- [87] C. V. Johnson, *Class. Quantum Grav.* **31**, 205002 (2014).
- [88] C. V. Johnson, *Class. Quantum Grav.* **33**, 215009 (2016).
- [89] R. A. Hennigar, F. McCarthy, A. Ballon, and R. B. Mann, *Class. Quantum Grav.* **34**, 175005 (2017).

- [90] H. Liu, and X. H. Meng, *Eur. Phys. J. C* **77**, 556 (2017).
- [91] B. Eslam Panah, *Phys. Lett. B* **787**, 45 (2018).
- [92] J. Zhang, Y. Li, and H. Yu, *Eur. Phys. J. C* **78**, 645 (2018).
- [93] S. H. Hendi, et al., *Phys. Lett. B* **781**, 40 (2018).
- [94] J. X. Mo, and S. Q. Lan, *Eur. Phys. J. C* **78**, 666 (2018).
- [95] A. Chakraborty, and C. V. Johnson, *Int. J. Mod. Phys. D* **28**, 1950006 (2019).
- [96] S. W. Wei, and Y. X. Liu, *Nucl. Phys. B* **946**, 114700 (2019).
- [97] L. Balart, and S. Fernando, *Phys. Lett. B* **795**, 638 (2019).
- [98] J. Zhang, Y. Li, and H. Yu, *JHEP* **02**, 144 (2019).
- [99] B. Eslam Panah, Kh. Jafarzade, and S. H. Hendi, *Nucl. Phys. B* **961**, 115269 (2020).
- [100] K.V. Rajani, et al., *Nucl. Phys. B* **960**, 115166 (2020).
- [101] H. Ghaffarnejad, E. Yaraie, M. Farsam, and K. Bamba, *Nucl. Phys. B* **952**, 114941 (2020).
- [102] C. Promsiri, E. Hirunsirisawat, and W. Liewriani, *Phys. Rev. D* **104**, 064004 (2021).
- [103] Y. Cao, H. Feng, J. Tao, and Y. Xue, *Gen. Relativ. Gravit.* **54**, 105 (2022).
- [104] B. Eslam Panah, and Kh. Jafarzade, *Gen. Relativ. Gravit.* **54**, 19 (2022).
- [105] M. C. DiMarco, S. L. Jess, R. A. Hennigar, and R. B. Mann, *Phys. Rev. D* **107**, 044001 (2023).
- [106] A. Eckart, R. Genzel, T. Ott, R. Schoedel, *Monthly Notices of the Royal Astronomical Society* **331**, 917 (2002).
- [107] S. Gillessen et al, *ApJ* **707**, L114 (2009).
- [108] B. Hamil, B. C. Lutfuoglu, *Eur. Phys. J. C* **85**, 313 (2025).
- [109] B. Hamil, B. C. Lutfuoglu, *Gen. Relativ. Gravit.* **57**, 140 (2025).
- [110] B. Hamil, Ahmad Al-Badawi, B. C. Lutfuoglu, *Phys. Scr.* **100**,105008 (2025).
- [111] Ahmad Al-Badawi, B. Hamil, *Int.J. Mod. Phys. D* **35**, 2550087 (2026).
- [112] B. Hamil, B. C. Lutfuoglu, *Chinese Physics C* **48**, 055102 (2024).
- [113] B. Hamil, B. C. Lutfuoglu, *Chinese Physics C* **49**, 025107 (2025).
- [114] E. Hackmann, C. Lammerzahl, *Phys. Rev. D* **78**, 024035 (2008).
- [115] M.Jamil, S. Hussain, B. Majeed, *Eur. Phys. J. C* **75**, 24 (2015).
- [116] S. Fernando, *Gen. Relativ. Gravit.* **44**, 1857 (2012).
- [117] J.L.Synge, *Ann. Math.* **35**, 705 (1934).
- [118] F.A.E. Pirani, *Acta Phys. Polon.* **15**, 389 (1956).
- [119] S.Ghosh, S. Kar, H. Nandan, *Phys. Rev. D* **82**, 024040 (2010).
- [120] R.Koley, S. Pal, S. Kar, *Am. J. Phys.* **71**, 1037 (2003).
- [121] R.Uniyal, H. Nandan, K.D.Purohit, *Mod. Phys. Lett. A* **29**, 1450157 (2014).
- [122] W. Cong, and R. B. Mann, *JHEP* **11**, 004 (2019).
- [123] C. V. Johnson, *Mod. Phys. Lett. A* **35**, 2050098 (2020).
- [124] M. Cvetič, G. W. Gibbons, D. Kubiznak, and C. N. Pope, *Phys. Rev. D* **84**, 024037 (2011).
- [125] R. Banerjee, S. K. Modak, and D. Roychowdhury, *JHEP* **10**, 125 (2012).
- [126] J. -X. Mo, and W. -B. Liu, *Phys. Lett. B* **727**, 336 (2013).
- [127] I. Prigogine, and R. Defay, *Chemical Thermodynamics*, Longmans Green, New York, 1954.
- [128] P. K. Gupta, and C. T. Moynihan, *J. Chem. Phys.* **65**, 4136 (1976).
- [129] R. Banerjee, S. K. Modak, and S. Samanta, *Eur. Phys. J. C* **70**, 317 (2010).
- [130] S. Chandrasekhar, "The mathematical theory of black holes", Oxford University Press, 2002.
- [131] M. Novello, V. A. De Lorenci, J. M. Salim et al., *Phys.Rev. D* **61**, 045001 (2000),
- [132] Dehyadegari, Amin, and Ahmad Sheykhi. "Reentrant phase transition of Born-Infeld-AdS black holes." *Physical Review D* **98** (2018): 024011.
- [133] Wei, Shao-Wen, Yu-Xiao Liu, and Robert B. Mann. "Black hole solutions as topological thermodynamic defects." *Physical Review Letters* **129** (2022): 191101.